AD-A080 355 VIRGINIA POLYTECHNIC INST AND STATE UNIV BLACKSBURG --ETC F/G 17/7
STAR PATTERN RECOGNITION AND SPACECRAFT ATTITUDE DETERMINATION.(U)
OCT 78 J L JUNKINS, T E STRIKWERDA DAAK70-78-C-0038
UNCLASSIFIED VPI-E-79-4 ETL-0173 NL

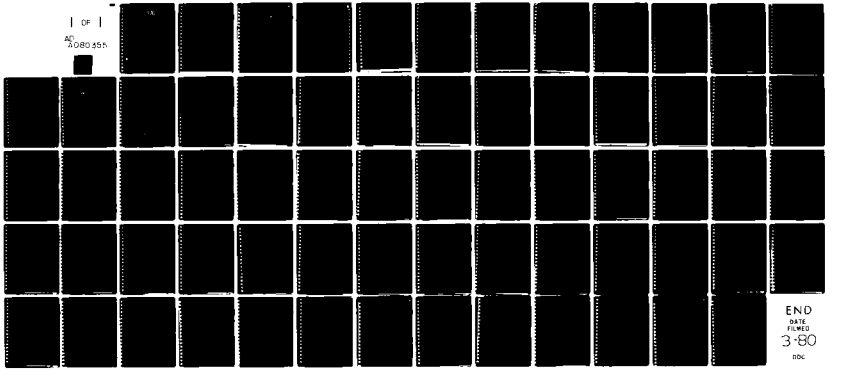

LEVEL II

U.S. Army Engineering Topographic Laboratories
Contractor Report Number

ETL-0173

STAR PATTERN RECOGNITION

AND

SPACECRAFT ATTITUDE DETERMINATION

PHASE I

Prepared By:

John L. Junkins
Thomas E. Strikwerda
L. Glenn Kraige

Engineering Science and Mechanics Department
Virginia Polytechnic Institute and State University
Blacksburg, Virginia 24061

ETL-0173

STAR PATTERN RECOGNITION

AND

SPACECRAFT ATTITUDE DETERMINATION

PHASE I

Prepared By:

John L. Junkins
Thomas E. Strikwerda
L. Glenn Kraige

Engineering Science and Mechanics Department
Virginia Polytechnic Institute and State University
Blacksburg, Virginia 24061

October 1978

Contributors:

Dr. John L. Junkins, Principal Investigator
Dr. L. Glenn Kraige, Co-Principal Investigator
Mr. Mahesh Rajan, Research Assistant
Dr. Thomas E. Strikwerda, Research Associate
Mr. James D. Turner, Research Assistant
Mr. Lawrence D. Ziems, Computer Programmer

Prepared For:

U.S. Army Engineer Topographic Laboratories
Fort Belvoir, Virginia 22060
Contract No. DAAK70-C-0038

VPI & SU Report No. VPI-E-79.4 Copy No. 24

20. (continued)

rate gyros are used to estimate motion continuously. Three intermittently communicating microcomputers operate in *parallel* to perform the functions: (i) star image centroid determination, (ii) star pattern identification and discrete attitude estimation (subsets of measured stars are identified as specific cataloged stars), (iii) optimal Kalman attitude motion estimation/integration. The system is designed to be self-calibrating with provision for routine updating of interlock angles, gyro bias parameters, and other system calibration parameters. For redundancy and improved precision, two optical ports are employed. This interim report documents Phase I of a three phase effort to research, develop, and laboratory test the basic concepts of this new system. Included in Phase I is definition, formulation, and test of the basic algorithms, including preliminary implementations and results from a laboratory microcomputer system.

TABLE OF CONTENTS

FOREWARD

This document represents an interim report covering Phase I (FY78) of Contract DAAK70-78-C-0038 issued by

Department of the Army
U.S. Army Mobility Equipment Research
and Development Command
Procurement and Production Directorate
Fort Belvoir, Virginia 22060

for the U.S. Army Engineer Topographic Laboratories (USAETL).

The authors appreciate the capable guidance of Mr. L. A. Gambino, Director of the Computer Science Laboratory (USAETL), who served as Technical Monitor for this effort. We also appreciate the technical liasion and contributions of Mr. Lon Smith (Defense Mapping Agency Headquarters).

SUMMARY

The primary results of the Phase I effort are the following:

1. Development of an approach for real time on-board estimation of spacecraft orientation with sub five arc-second precision.

2. Detailed formulation, tests and validations of an efficient and reliable star pattern recognition strategy appropriate for use with charged-coupled-device (CCD) array-type star sensors.

3. Formulation and preliminary tests of a motion integration/ Kalman filter algorithm to integrate gyro measured angular rates and (by sequential processing of the discrete orientation information available from the star sensing, identification, and attitude determination process) provide optimal real time estimates of spacecraft orientation and angular velocity.

4. Definition of software and hardware for a laboratory microcomputer-system-based study to permit realistic ground-based validation and optimization of the algorithms and computer configuration.

These results are discussed in detail herein.

1.0 INTRODUCTION AND SYSTEM OVERVIEW

The purpose of the research activities reported upon herein is to research and develop a system which has potentially profound impact upon satellite-based technologies requiring precision knowledge (sub-five-arc- second uncertainty) of spacecraft attitude.

The focus of the research has been the optimal exploitation of array-type Charged Coupled Devices (CCD) as the star light sensitive element in a new generation of star sensing and star pattern recognition systems; these systems hold the promise of autonomous, on-board, near-real-time determination of spacecraft attitude, with state-of-the-art precision[1-3]. The heart of the measurement hardware designs (several similar configurations are currently under development and test) is a CCD array or matrix of about 200,000 light-sensitive elements, accurately imbedded (to 1 part in 10,000) in a microcircuit chip. The CCD array serves as the "film" of a new generation of "digital stellar cameras" which can accurately digitize star images with negligible lag from real time. The digitized starlight is analyzed by a programmable microprocessor which extracts star image coordinates and magnitudes and associates a time with these measurements. The microprocessor outputs star image and magnitude data in near-real time (current projections indicate 5 or more star "photographs" per minute). The measured star patterns output from the microprocessor can be telemetered to ground, but ultimately, it appears feasible to use methods described herein to determine spacecraft orientation from these data with sub-five-arc-second precision, within the constraints of on-board computation, and thereby open the door for a truly dramatic breakthrough.

With reference to Figures 1.1, 1.2, and 1.3, we discuss a modular parallel process approach to the attitude determination problem. There are four major sub-systems, viz:

(1) Two CCD matrix arrays and associated electro-optics for sensing and digitizing starlight. Two identical optical ports having effective focal lengths of about 70 mm focus starlight from 7° x 9° fields of view onto the CCD arrays. The fields of view can be separated by any convenient angle, but we have nominally used 90°. The CCD arrays are taken as Fairchild's 11.4 mm x 8.8 mm matrix arrays containing a grid of 488 x 380 silcon pixels. The starlight is slightly defocused on the CCD image planes (to facilitate more accurate "centroiding" of image locations); typical stars illuminate 16 to 25 pixels. The image processing takes place in two stages. The first stage is a high speed analog scan to identify the pixel addresses and A/D convert the response levels which are greater than a preset analog level. The analog scans for the two fields of view are controlled by a common clock to make the digitized data valid at the same instant.

(2) Microprocessor A performs the program Process A, which is the digital portion of the image process function. Process A is a sequence of calculations/logical decisions requiring as input the A/D converted response levels, pixed addresses, and time from the CCD response. The output data of Process A are the interpolated image centroids and instrument (relative) magnitudes of each valid star image. An average of about six stars will be detected on each CCD array. Upon ouput from Process A, the star image centroids will have been enhanced by all

preflight calibration data, and any easily detectable spurious images will have been deleted. The time recorded when the data were scanned from the CCD arrays remains associated with data and is transmitted along with the image centroids and magnitudes to Process A's output queue. The output queue of Process A will be continuously accessible by Process B and/or telemetry systems; the information will be updated (over-written) at a to-be-determined interval (about five times per minute). The data compression affected by immediate extraction of image centroids and magnitudes from the pixel response (and, by virtue of the high speed analog scan, considering only the significantly illuminated pixels) is most important to the concept of an autonomous on board system; the transmission, storage, and subsequent analysis of the large volume of pixel data is thereby made unnecessary.

(3) Microprocessor B is programmed to execute Process B which accepts as inputs:

- apriori attitude estimates,
- apriori estimation of interlock angles between the two image planes
- star image coordinates and magnitude data, usually one data set from each CCD array, from Process A (port II).

Through a sequence of calculations/decisions (including systematic access of a star catalog containing the direction cosines and magnitudes of the 5000 brightest stars), Process B performs two primary functions:

- Identifies the measured stars in each field of view-of-view as specific cataloged stars (using a "star pair correlation" technique), and

- Determines the spacecraft orientation angles and field-of-view interlock angles (which causes the simulated images of identified stars to overlay the measured images in the least square sense).

The spacecraft orientation output from Process B will be available continuously, and will nominally be updated two or more times per minute. As soon as the attitude determination process is completed, the previous attitude angles and associated time are overwritten by the new attitude angles and times (at data port III, at a nominal rate of 2 or more readouts per minute).

(4) Microprocessor C is programmed to accept the discretely valid attitude determinations of Process B and A/D converted gyro measurements of angular velocity to determine a best real time attitude and angular velocity estimates for possible feedback to the control system, for feedback to Process B, and for telemetry to ground.

In Phase I (just completed) of this research and development effort, we have concentrated upon the following tasks:

(1) Development and test of methods and algorithms for Process B, for star pattern recognition and attitude determination.

(2) Development and test of methods and algorithms for Process C, for continuous real time attitude estimation from Process B discrete attitude estimates and rate gyro measurements.

(3) Evaluating the designs and error characteristics of competing CCD star tracker designs, in order to develop realistic CCD output simulations for input to Process A and B.

(4) Simulation of instrument response characteristics on the CCD array, centroiding errors, etc.

(5) Creation of mission star catalogs.

(6) Identification of requirements for a microcomputer system to conduct tests of Processes B and C within the precision, speed, and storage constraints of an on-board computer.

To date, the overwhelming majority of the computational studies have been carried out on the VPI & SU IBM 370/158 computer system. However, we have recently begun conversions and report some limited results of studies done on a HP 9845S microcomputer system. During Phase II, both Processes B and C will be implemented on this computer.

In the text of this report, we discuss the above tasks and their results, status, and outlook for Phases II and III.

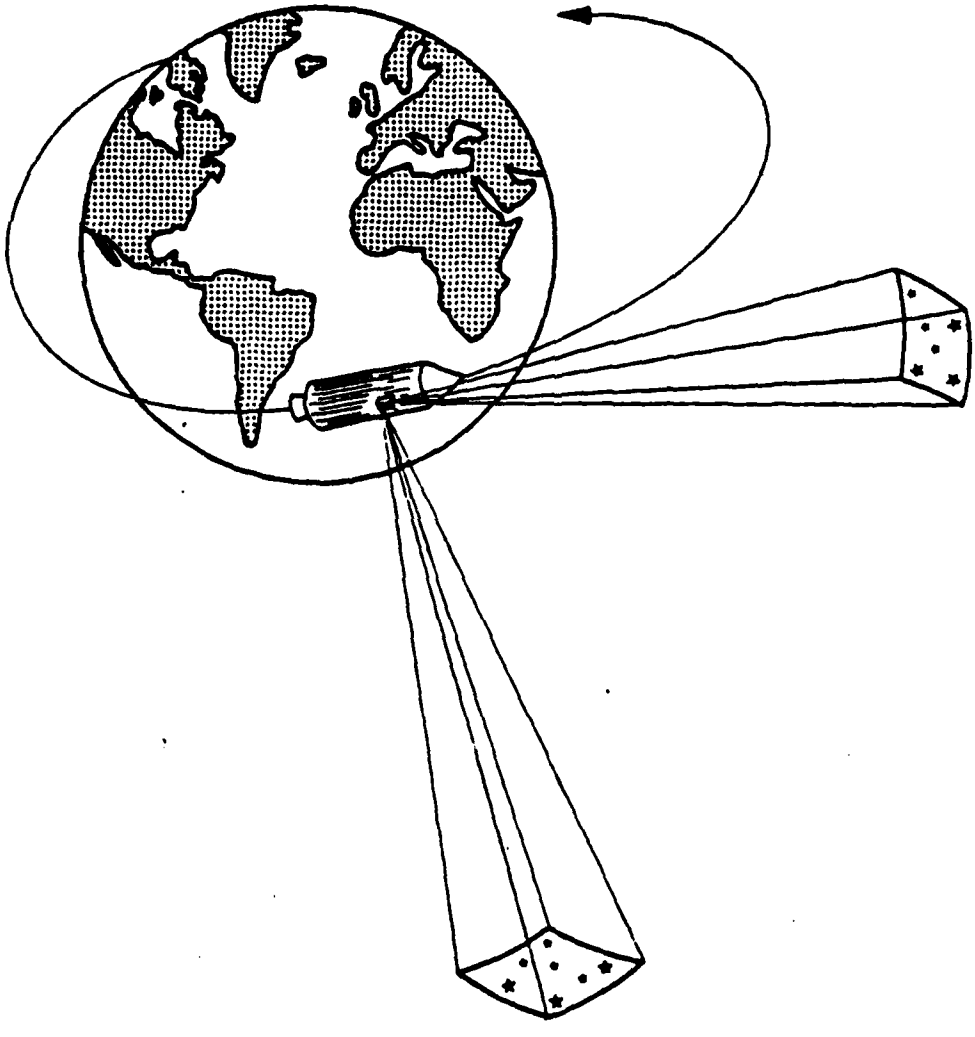

FIGURE 1.1 UVASTAR An electro-optical/software system capable of real time readout of digitized star coordinates, and ultimately, autonomous, near-real time star pattern recognition and attitude determination.

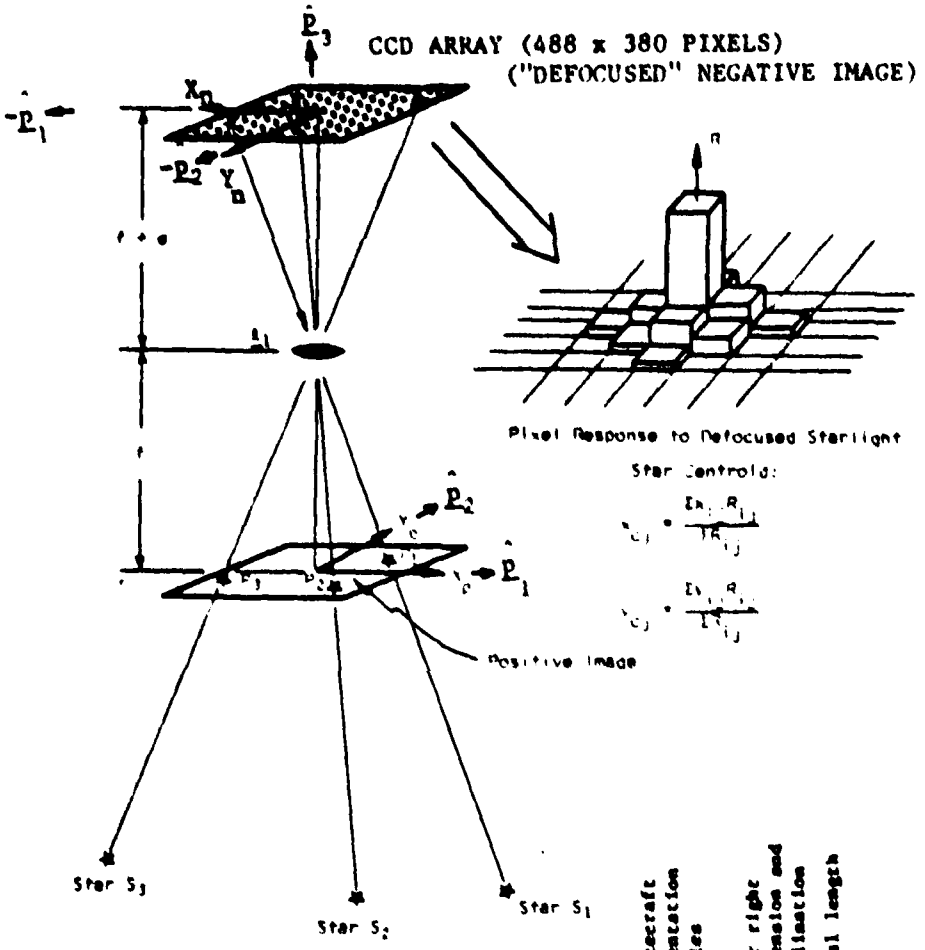

Colinearity Equations:

$$X_n = f\left[\frac{C_{11}L_1 + C_{12}L_2 + C_{13}L_3}{C_{31}L_1 + C_{32}L_2 + C_{33}L_3}\right] = \text{function}\ (\underbrace{\phi, \theta, \psi}_{\text{Spacecraft Orientation Angles}}, \underbrace{\alpha, \delta}_{\text{Star right Ascension and Declination}}, \underbrace{f}_{\text{Focal length}})$$

$$Y_n = f\left[\frac{C_{21}L_1 + C_{22}L_2 + C_{23}L_3}{C_{31}L_1 + C_{32}L_2 + C_{33}L_3}\right] = \text{function}\ (\phi, \theta, \psi, \alpha, \delta, f)$$

where

$$\left.\begin{aligned} L_1 &= \cos\delta\cos\alpha \\ L_2 &= \cos\delta\sin\alpha \\ L_3 &= \sin\delta \end{aligned}\right\} \text{ star direction cosines, } [C_{ij}] = \begin{bmatrix} \cos\psi & \sin\psi & 0 \\ -\sin\psi & \cos\psi & 0 \\ 0 & 0 & 1 \end{bmatrix} \begin{bmatrix} \cos\theta & 0 & -\sin\theta \\ 0 & 1 & 0 \\ \sin\theta & 0 & \cos\theta \end{bmatrix} \begin{bmatrix} 1 & 0 & 0 \\ 0 & \cos\phi & \sin\phi \\ 0 & -\sin\phi & \cos\phi \end{bmatrix}$$

FIGURE 1.2: Formation of Image on the CCD Array.

FIGURE 1.3

STAR PATTERN RECOGNITION/SPACECRAFT ATTITUDE ESTIMATION

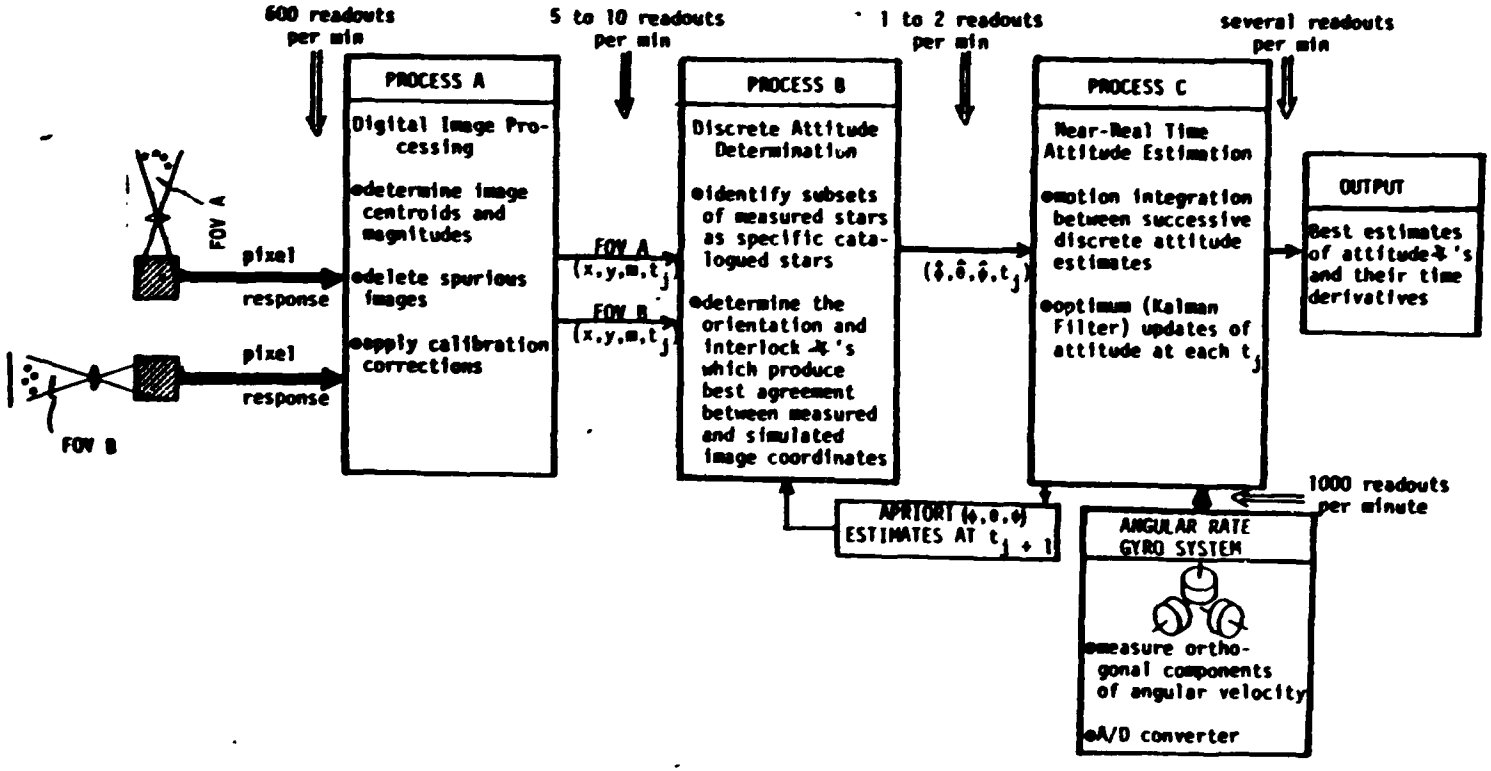

2.0 COORDINATE FRAME NOMENCLATURE AND KINEMATICAL RELATIONSHIPS

Important to any complex angular motion problem is the choice of orientation parameters and a clear, systematic nomenclature convention. The choice of orientation parameters is critical in that numerical difficulties may be avoided entirely or at least relegated to attitudes which will never occur in the problem at hand; a self-evident nomenclature is useful (particularly when several coordinate systems are defined) not only to readers but to the investigators themselves.

Throughout Phase I of this research effort, Euler angles have been utilized for coordinate frame orientation. It is a well-known fact that each of the twelve possible Euler angle sets possesses a kinematical singularity. In order to render the singularity problem as harmless as possible, the Euler angle sequence for a given coordinate frame relative orientation has been selected so that encountering the singular orientation is highly unlikely. Future efforts may involve the use of a four parameter orientation description (such as Euler parameters) so as to avoid the singularity problem entirely.

Unless there are reasons to the contrary, the 1-2-3 Euler angle sequence will be preferred. For future reference, the 3 x 3 transformation matrix [DE] orienting a frame D characterized by the orthonormal vector set

$$\{\underline{d}\} = \begin{Bmatrix} \underline{d}_1 \\ \underline{d}_2 \\ \underline{d}_3 \end{Bmatrix} \tag{2.1}$$

relative to a frame E characterized by

$$\{\underline{e}\} = \begin{Bmatrix} \underline{e}_1 \\ \underline{e}_2 \\ \underline{e}_3 \end{Bmatrix} \tag{2.2}$$

has the form

$$[DE(\phi_{de},\theta_{de},\psi_{de})] = \begin{bmatrix} c\psi_{de} & s\psi_{de} & 0 \\ -s\psi_{de} & c\psi_{de} & 0 \\ 0 & 0 & 1 \end{bmatrix} \begin{bmatrix} c\theta_{de} & 0 & -s\theta_{de} \\ 0 & 1 & 0 \\ s\theta_{de} & 0 & c\theta_{de} \end{bmatrix} \begin{bmatrix} 1 & 0 & 0 \\ 0 & c\phi_{de} & s\phi_{de} \\ 0 & -s\phi_{de} & c\phi_{de} \end{bmatrix} \quad (2.3)$$

where ϕ_{de}, θ_{de}, and ψ_{de} are the 1-2-3 Euler angles shown in Fig. 2.1 and $c\theta_{de} = \cos\theta_{de}$, $s\theta_{de} = \sin\theta_{de}$, etc. The relationship between the two frames is compactly written as the matrix product

$$\{\underline{d}\} = [DE(\phi_{de},\theta_{de},\psi_{de})]\{\underline{e}\}. \quad (2.4)$$

Obtainable from an elementary kinematic analysis of the frames displayed in Fig. 2.1 is the following matrix expression for the components (along the $\{\underline{d}\}$ unit vectors) of the angular velocity of frame D with respect to frame E:

$$\begin{Bmatrix} \omega_1^{D/E} \\ \omega_2^{D/E} \\ \omega_3^{D/E} \end{Bmatrix} = \begin{bmatrix} c\theta_{de}c\psi_{de} & s\psi_{de} & 0 \\ -c\theta_{de}s\psi_{de} & c\psi_{de} & 0 \\ s\theta_{de} & 0 & 1 \end{bmatrix} \begin{Bmatrix} \dot{\phi}_{de} \\ \dot{\theta}_{de} \\ \dot{\psi}_{de} \end{Bmatrix} \quad (2.5)$$

Finally, both members of Eq. (2.5) may be premultiplied by the inverse of the 3 x 3 matrix on the right hand side to obtain expressions for the time rates of change of the Euler angles:

$$\begin{Bmatrix} \dot{\phi}_{de} \\ \dot{\theta}_{de} \\ \dot{\psi}_{de} \end{Bmatrix} = \frac{1}{c\theta_{de}} \begin{bmatrix} c\psi_{de} & -s\psi_{de} & 0 \\ c\theta_{de}s\psi_{de} & c\theta_{de}c\psi_{de} & 0 \\ s\theta_{de}c\psi_{de} & s\theta_{de}c\psi_{de} & c\theta_{de} \end{bmatrix} \begin{Bmatrix} \omega_1^{D/E} \\ \omega_2^{D/E} \\ \omega_3^{D/E} \end{Bmatrix} = [B(\theta_{de},\psi_{de})] \begin{Bmatrix} \omega_1^{D/E} \\ \omega_2^{D/E} \\ \omega_3^{D/E} \end{Bmatrix} \quad (2.6)$$

Contained in the above discussion are sub-and superscript conventions which, while appearing unnecessary in this simple context, will be utilized to great advantage in conjunction with the several coordinate frames about to be introduced.

We now turn to the first of the specific coordinate frames selected for use in the present problem. The inertial frame N (see Fig. 2.2) is non-rotating

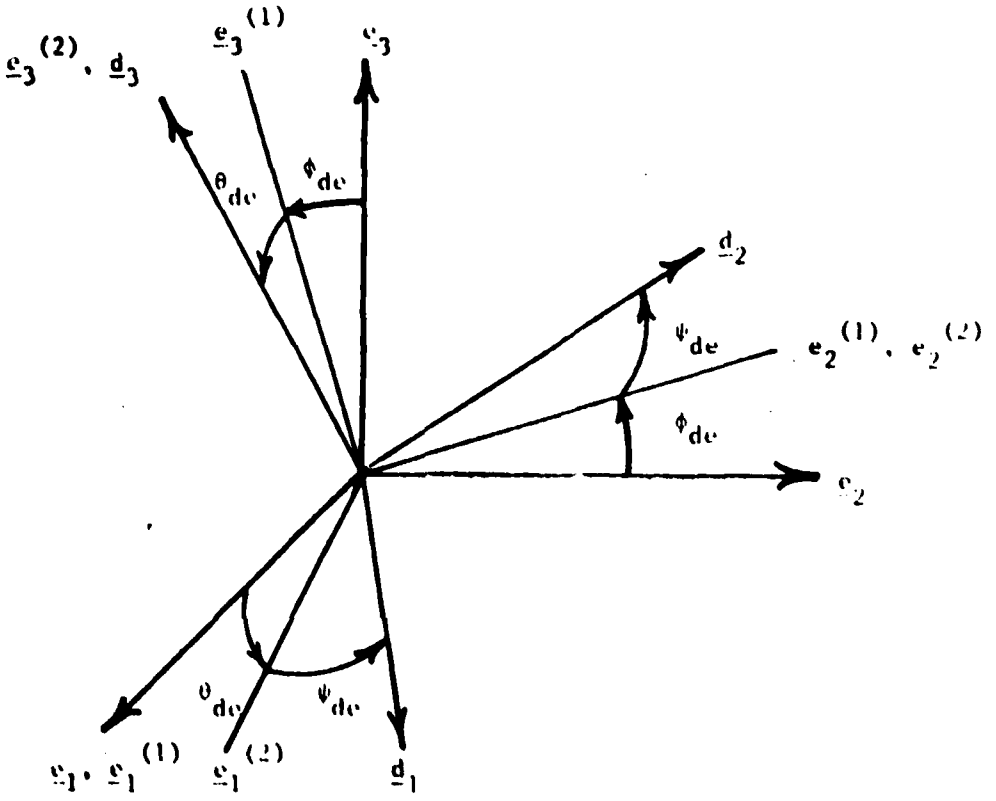

Fig. 2.1: A 1-2-3 Euler Angle Transformation

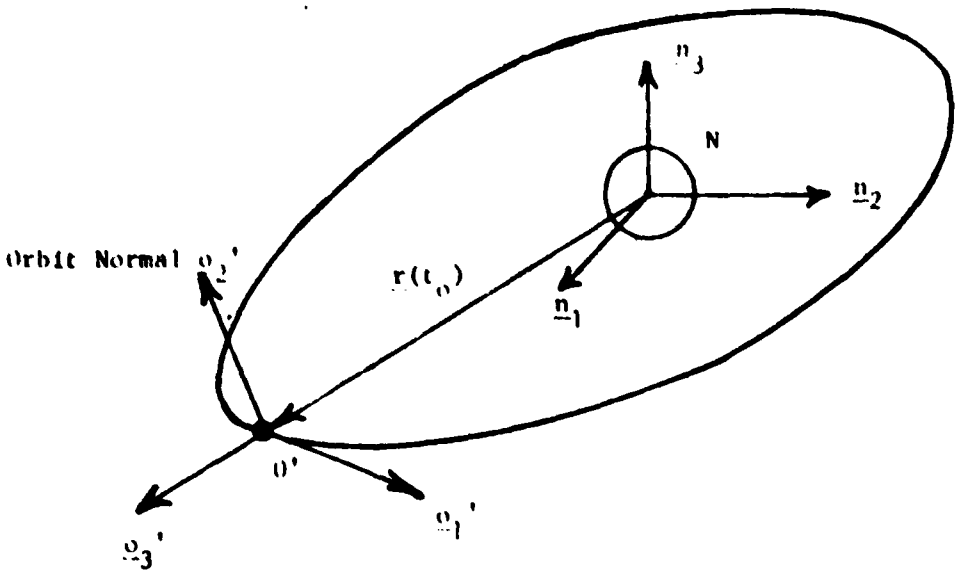

Fig. 2.2: The Inertial (N) and Orbit Inertial (O') Frames

and geocentric; it forms the basis for the on-board star catalog and is characterized by the unit vector set

$$\underline{n} = \begin{Bmatrix} \underline{n}_1 \\ \underline{n}_2 \\ \underline{n}_3 \end{Bmatrix} \tag{2.7}$$

An "orbit inertial" frame O' (see Fig. 2.2) is defined by the unit vectors

$$\begin{aligned} \underline{o}'_3 &= \frac{\underline{r}_o}{r_o} \\ \underline{o}'_2 &= \frac{\underline{r}_o \times \underline{r}_o}{|\underline{r}_o \times \underline{r}_o|} \\ \underline{o}'_1 &= \underline{o}'_2 \times \underline{o}'_3, \end{aligned} \tag{2.8}$$

where the subscript o denotes initial conditions. The $\{\underline{o}'\}$ unit vectors are projected onto the $\{\underline{n}\}$ unit vectors by the direction cosine matrix [O'N] as

$$\{\underline{o}'\} = [O'N]\{\underline{n}\} \tag{2.9}$$

The nine constant elements of [O'N] are calculated from the orbit state vector by

$$\begin{aligned} O'N_{31} &= \frac{x_o}{r_o} \\ O'N_{32} &= \frac{y_o}{r_o} \\ O'N_{33} &= \frac{z_o}{r_o} \\ O'N_{21} &= \frac{h_1}{h} \\ O'N_{22} &= \frac{h_2}{h} \\ O'N_{23} &= \frac{h_3}{h} \\ O'N_{11} &= O'N_{22}O'N_{33} - O'N_{23}O'N_{32} \\ O'N_{12} &= O'N_{23}O'N_{31} - O'N_{21}O'N_{33} \\ O'N_{13} &= O'N_{21}O'N_{32} - O'N_{22}O'N_{31}, \end{aligned} \tag{2.10}$$

where $h_1 = (y_o\dot{z}_o - z_o\dot{y}_o)$

$h_2 = (z_o\dot{x}_o - x_o\dot{z}_o)$ (2.11)

$h_3 = (x_o\dot{y}_o - y_o\dot{x}_o)$

$h = (h_1^2 + h_2^2 + h_3^2)^{1/2}$

The orbit frame O (see Fig. 2.3) rotates about $\underline{o}_2'$, the orbit normal, with the constant angular velocity (relative to N or O')

$$\underline{\omega}^{O/N} = \underline{\omega}^{O/O'} = \Omega\underline{o}_2' = \Omega\underline{o}_2, \tag{2.12}$$

where Ω is given by

$$\Omega = \frac{2\pi}{\text{(orbit period)}} = \frac{2\pi}{\sqrt{GM}}\, a^{3/2}. \tag{2.13}$$

GM is the earth gravitational-mass constant and a is the semi-major axis of the orbit. The $\{\underline{o}\}$ unit vectors are written in terms of the $\{\underline{o}'\}$ unit vectors by

$$\{\underline{o}\} = [OO'(t)]\{\underline{o}'\}, \tag{2.14}$$

where

$$[OO'(t)] = \begin{bmatrix} \cos[\Omega(t - t_o)] & 0 & -\sin[\Omega(t - t_o)] \\ 0 & 1 & 0 \\ \sin[\Omega(t - t_o)] & 0 & \cos[\Omega(t - t_o)] \end{bmatrix} \tag{2.15}$$

Substitution of Eq. (2.9) into Eq. (2.14) yields

$$\{\underline{o}\} = [OO'(t)][O'N]\{\underline{n}\} \tag{2.16}$$

The next coordinate frame (G) considered is one attached to the strapped-down gyroscopic assembly and hence body-fixed but not necessarily principal. The G frame is generally considered to be the primary spacecraft axes. The unit vector set $\{\underline{g}\}$ of Fig. 2.3 is characterized by $\underline{g}_1$ being the roll axis (nominally along the velocity vector), $\underline{g}_2$ being the pitch axis (nominally along the orbit normal), and $\underline{g}_3$ being the yaw axis (nominally along the radius vector). The 1-2-3 angles ϕ_{go}, θ_{go}, and ψ_{go} orienting G relative to O are hence normally small, thereby avoiding the kinematical singularity at

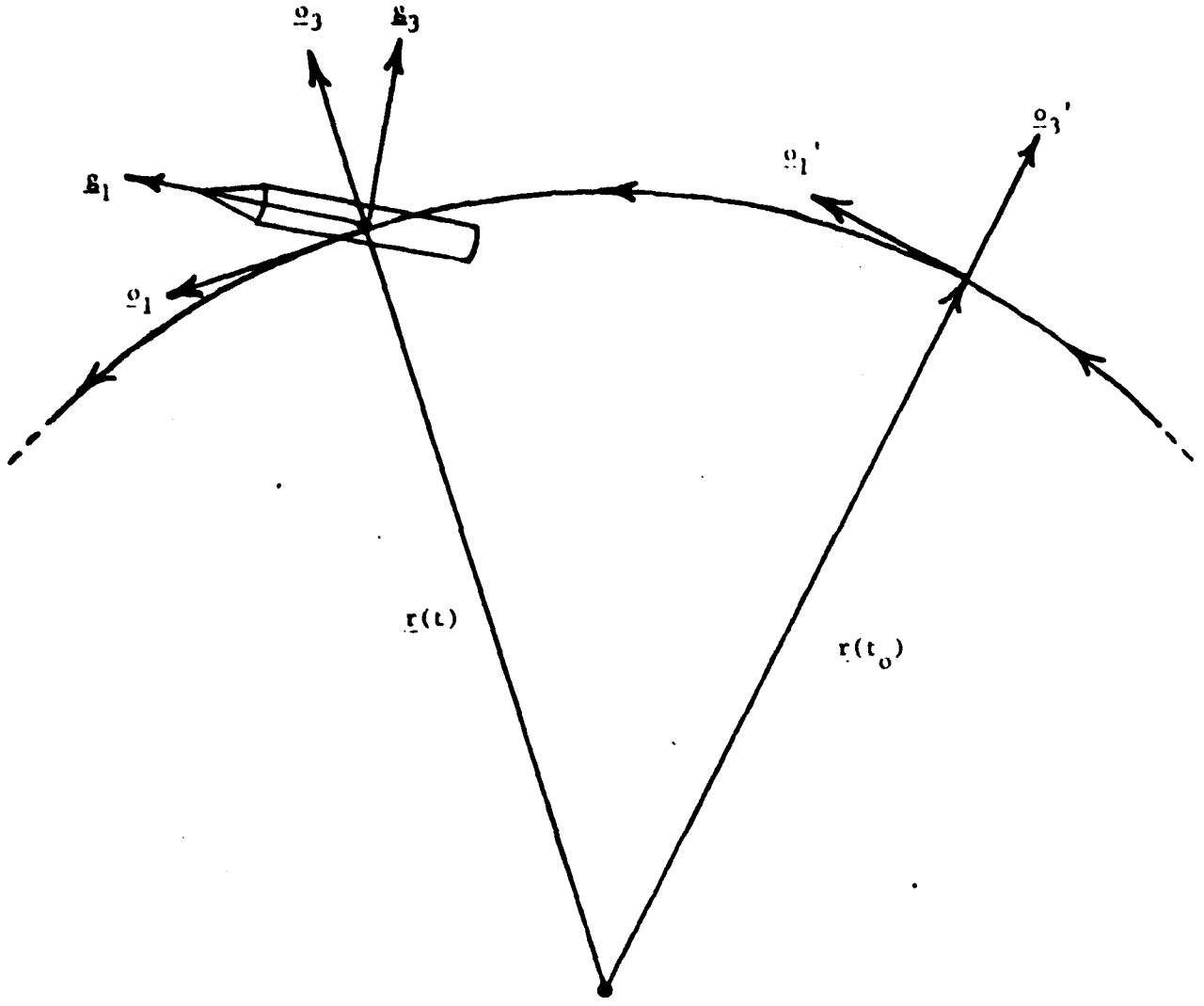

Fig. 2.3: The Orbit Frame O and Gyroscopic Frame G

$\theta_{go} = 90°$. The $\{\underline{g}\}$ unit vectors are projected onto the $\{\underline{o}\}$ unit vectors by

$$\{\underline{g}\} = [GO(\phi_{go},\theta_{go},\psi_{go})]\{\underline{o}\}. \tag{2.17}$$

Utilizing Eq. (2.16):

$$\{\underline{g}\} = [GO][OO'][O'N]\{\underline{n}\}. \tag{2.18}$$

We now introduce the frames A and B associated with the star sensor fields-of-view A and B. Frame A (see Fig. 2.4) is characterized by $\underline{a}_3$ being along the field-of-view A boresight, with $\underline{a}_1$ and $\underline{a}_2$ being image plane axes. The angles ϕ_{ag}, θ_{ag}, and ψ_{ag} orient the $\{\underline{a}\}$ unit vectors relative to $\{\underline{g}\}$ via the 3-1-3 rotation

$$\{\underline{a}\} = [AG(\phi_{ag},\theta_{ag},\psi_{ag})]\{\underline{g}\} \tag{2.19}$$

$$= [AG][GO]\{\underline{o}\} \tag{2.20}$$

$$= [AG][GO][OO']\{\underline{o}'\} \tag{2.21}$$

$$= [AG][GO][OO'][O'N]\{\underline{n}\}. \tag{2.22}$$

A 3-1-3 sequence has been chosen for this orientation interlock, with the nominal values

$$(\phi_{ag},\theta_{ag},\psi_{ag}) = (90°,135°,0°). \tag{2.23}$$

Frame B, for purpose of recovering the interlock angle between fields-of-view A and B, is oriented relative to frame A by the 3-1-3 angles ϕ_{ba},θ_{ba}, and ψ_{ba} via

$$\{\underline{b}\} = [BA(\phi_{ba},\theta_{ba},\psi_{ba})]\{\underline{a}\}. \tag{2.24}$$

For our study, the interlock angles have been assigned the nominal values (see Fig. 2.4).

$$(\phi_{ba},\theta_{ba},\psi_{ba}) = (-90°,\ 90°,\ 90°). \tag{2.25}$$

The orientations prescribed by Eqs. (2.23) and (2.25) correspond to $\underline{a}_3$ (the field-of-view A boresight) being "yawed" about $\underline{g}_3$ by 45° from $\underline{g}_1$, and $\underline{b}_3$

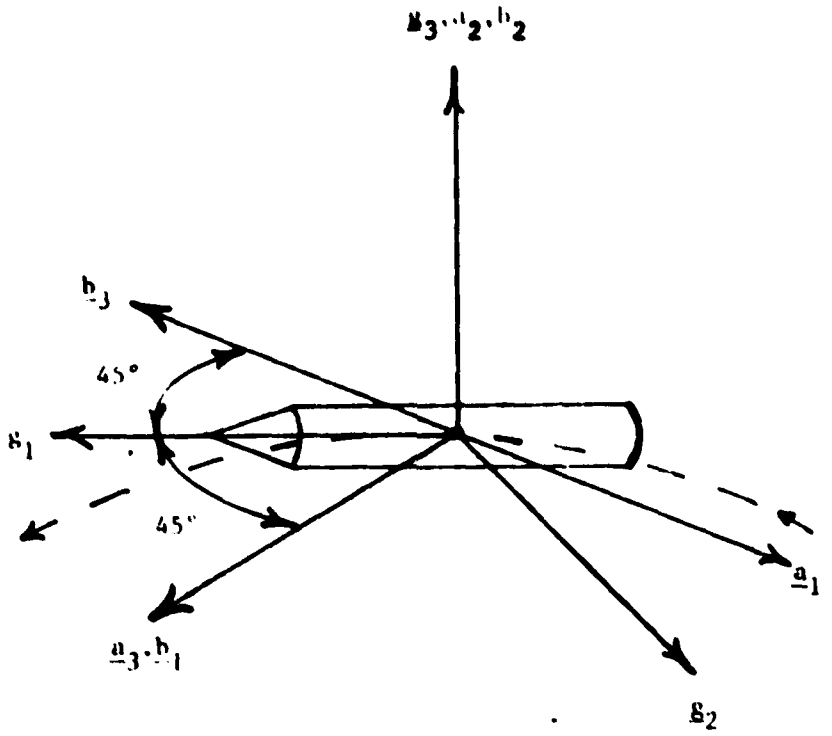

Fig. 2.4: The Field-of-View Frames A and B

(the field-of-view B boresight) being "yawed" about $\underline{g}_3$ by -45°.

Finally, we introduce an "orbit A frame", designated A', which is coincident with frame A at the initial time t_o, but which thereafter rotates about the orbit normal $\underline{o}_2 = \underline{o}_2'$ with the constant angular velocity

$$\underline{\omega}^{A'/N} = \underline{\omega}^{A'/O'} = \Omega \underline{o}_2' = \Omega \underline{o}_2. \tag{2.26}$$

Frame A' represents the nominal position of frame A and is oriented relative to frame O via

$$\{\underline{a}'\} = [A'O(\phi_{a'o}, \theta_{a'o}, \psi_{a'o})]\{\underline{o}\}, \tag{2.27}$$

Where the 1-2-3 Euler angles $\phi_{a'o}$, $\theta_{a'o}$, and $\psi_{a'o}$ are constants. The relationship between the frames A and A' is given by

$$\{\underline{a}\} = [AA'(\phi_{aa'}, \theta_{aa'}, \psi_{aa'})]\{\underline{a}'\}, \tag{2.28}$$

wherein the three 1-2-3 angles $\phi_{aa'}$, $\theta_{aa'}$, and $\psi_{aa'}$ are normally small.

Table 1 summarizes the coordinate system definitions and relationships discussed thus far.

The interlock angles (ϕ_{ag}, θ_{ag}, ψ_{ag}) and (ϕ_{ba}, θ_{ba}, ψ_{ba}) will vary about their nominal calibrated values due to thermal cycling or any other structural deformation. The maximum amplitude of such variations is believed to be a few arc-minutes. As is evident in the developments of Sections 3 and 4, it is possible to update the estimates of the interlock angles (ϕ_{ba}, θ_{ba}, ψ_{ba}) between the star sensor coordinate systems. However, we have not yet structured the estimation algorithms of Process C to provide correction of the interlock angles (ϕ_{ag}, θ_{ag}, ψ_{ag}). It is believed that noise in typical rate data (around one arc-sec/sec) is too large to allow significant refinement of (ϕ_{ag}, θ_{ag}, ψ_{ag}) unless Processes B and C can be implemented in such a fashion that several Process B outputs per minute can be passed through the Kalman filter of Process C. As is noted in Section 4, these interlock angles are correlated with the estimated rate bias parameters, a fact which also hampers accurate estimation.

Table 1. REFERENCE FRAME SUMMARY

Designation	Unit Vectors	Associated With	Comments	Most Common Projections
N	$\{\underline{n}\}$	Inertial Frame	Basis of on-board star catalog	
O'	$\{\underline{o}'\}$	"Orbit Inertial" Frame	Coincides with O at the initial time t_o	$\{\underline{o}'\} = [O'N]\{\underline{n}\}$
O	$\{\underline{o}\}$	Uniform rotation about orbit normal	Rotation Ω is about $\underline{o}_2 = \underline{o}'_2$, the orbit normal	$\{\underline{o}\} = [OO']\{\underline{O}'\}$ $= [OO'][O'N]\{\underline{n}\}$ $= [ON]\{\underline{n}\}$
G	$\{\underline{g}\}$	Gyro-fixed axes	$\underline{g}_1$: roll axis $\underline{g}_2$: pitch axis $\underline{g}_3$: yaw axis	$\{\underline{g}\} = [GO]\{\underline{O}\}$ $= [GO][OO'][O'M]\{\underline{n}\}$ $= [GN]\{\underline{n}\}$
A	$\{\underline{a}\}$	Field-of-view A	$\underline{a}_3$: along boresight $\underline{a}_1, \underline{a}_2$: image plane axes	$\{\underline{a}\} = [AG]\{\underline{g}\}$ $= [AG][GO][OO'][O'N]\{\underline{n}\}$ $= [AN]\{\underline{n}\}$ also, $\{\underline{a}\} = [AA']\{\underline{a}\}$
B	$\{\underline{b}\}$	Field-of-view B	b_3: along boresight b_1, b_2: image plane axes	$\{\underline{b}\} = [BA]\{\underline{a}\}$ $= [BA][AN]\{\underline{n}\}$ $= [BN]\{\underline{n}\}$
A'	$\{\underline{a}'\}$	Uniform rotation of initial A frame about orbit normal	Rotation Ω is about $\underline{O}_2 = \underline{O}'_2$, the orbit normal; $[A'O] = [AO(t_o)]$	$\{\underline{a}'\} = [A'O]\{\underline{O}\}$ $= [A'O][\overline{ON}]\{\underline{n}\}$ $= [A'N]\{\underline{n}\}$.

Useful for consideration in Process C (see Section 4) are the time rates of change of various Euler angle sets in terms of the inertial angular velocity components of frame G. Specifically, we will develop expressions for

(1) $(\dot{\phi}_{gn}, \dot{\theta}_{gn}, \dot{\psi}_{gn})$

(2) $(\dot{\phi}_{an}, \dot{\theta}_{an}, \dot{\psi}_{an})$

(3) $(\dot{\phi}_{go}, \dot{\theta}_{go}, \dot{\psi}_{go})$

(4) $(\dot{\phi}_{aa'}, \dot{\theta}_{aa'}, \dot{\psi}_{aa'})$.

The relationships for the time rates of change of the angles ϕ_{gn}, θ_{gn}, and ψ_{gn} follow directly from the form of Eqs. (2.6):

$$\begin{Bmatrix} \dot{\phi}_{gn} \\ \dot{\theta}_{gn} \\ \dot{\psi}_{gn} \end{Bmatrix} = \frac{1}{c\theta_{gn}} \begin{bmatrix} c\psi_{gn} & -s\psi_{gn} & 0 \\ c\theta_{gn}s\psi_{gn} & c\theta_{gn}c\psi_{gn} & 0 \\ s\theta_{gn}c\psi_{gn} & s\theta_{gn}c\psi_{gn} & c\theta_{gn} \end{bmatrix} \begin{Bmatrix} \omega_1^{G/N} \\ \omega_2^{G/N} \\ \omega_3^{G/N} \end{Bmatrix} = [B(\theta_{gn}, \psi_{gn})] \begin{Bmatrix} \omega_1^{G/N} \\ \omega_2^{G/N} \\ \omega_3^{G/N} \end{Bmatrix}. \quad (2.29)$$

Note that θ_{gn}, for the case of a near circular orbit and one vehicle rotation about $\underline{g}_2$ per orbit, will go to 90° twice per orbit, causing $\cos\theta_{gn}$ to vanish with a resulting singularity in Eqs. (2.29).

The relationships for the time rates of change of the angles ϕ_{an}, θ_{an}, and ψ_{an} can also be obtained from Eq. (2.6):

$$\begin{Bmatrix} \dot{\phi}_{an} \\ \dot{\theta}_{an} \\ \dot{\psi}_{an} \end{Bmatrix} = [B(\theta_{an}, \psi_{an})][AG(\phi_{ag}, \theta_{ag}, \psi_{ag})] \begin{Bmatrix} \omega_1^{G/N} \\ \omega_2^{G/N} \\ \omega_3^{G/N} \end{Bmatrix} \quad (2.30)$$

The factor of [AG] on the right side of Eq. (2.30) is necessary to convert the $\omega_i^{G/N}$ from components along $\{\underline{g}\}$ axes to components along $\{\underline{a}\}$ axes. Due to the form of the matrix B (defined in Eq. (2.6) and repeated in Eq. (2.29), singularities would occur twice per orbit for a vehicle which

rotates about $\underline{g}_2$ once per orbit. Hence, although fairly simple in form, Eqs. (2.29) and (2.30) share similar difficulties.

We now proceed to develop equations analogous to (2.29) and (2.30) for the angles (ϕ_{go}, θ_{go}, ψ_{go}) (Case 3). The angular velocity of G relative to N may be written as

$$\underline{\omega}G/N = \underline{\omega}G/O + \omega O/N \tag{2.31}$$

or

$$\omega_1 G/N \underline{g}_1 + \omega_2 G/N \underline{g}_2 + \omega_3 G/N \underline{g}_3 = \dot{\phi}_{go}\underline{o}_1^{(1)} + \dot{\theta}_{go}\underline{o}_2^{(2)} + \dot{\psi}_{go} + \Omega\underline{o}_2, \tag{2.32}$$

where the parenthetical superscripts indicate intermediate frames in the O to G transformation. Expressing $\underline{o}_1^{(1)}$, $\underline{o}_2^{(2)}$, and $\underline{o}_2$ in terms of $\underline{g}_1$, $\underline{g}_2$, and $\underline{g}_3$ enables one to equate coefficients of like unit vectors, resulting in three scalar equations which have the matrix form

$$\begin{Bmatrix} \dot{\phi}_{go} \\ \dot{\theta}_{go} \\ \dot{\psi}_{go} \end{Bmatrix} = [B(\theta_{go},\psi_{go})] \begin{Bmatrix} \omega_1^{G/N} \\ \omega_2^{G/N} \\ \omega_3^{G/N} \end{Bmatrix} - \Omega \begin{Bmatrix} c\phi_{go}s\psi_{go} + s\phi_{go}s\theta_{go}c\psi_{go} \\ c\phi_{go}c\psi_{go} - s\phi_{go}s\theta_{go}s\psi_{go} \\ -s\phi_{go}c\theta_{go} \end{Bmatrix} \tag{2.33}$$

For the case of one vehicle rotation about $\underline{g}_2$ per near circular orbit, the angles ϕ_{go}, θ_{go}, and ψ_{go} remain small so that Eqs. (2.33) are non-singular and nearly linear (important in the implementation of estimation algorithms).

To develop the Case 4 equations for $\dot{\phi}_{aa'}$, $\dot{\theta}_{aa'}$, and $\dot{\psi}_{aa'}$, we begin with

$$\underline{\omega}^{G/N} = \underline{\omega}^{A/A'} + \underline{\omega}^{A'/N}. \tag{2.34}$$

Proceeding in a manner analogous to that outlined for Case 3, we arrive at

$$\begin{Bmatrix} \dot{\phi}_{aa'} \\ \dot{\theta}_{aa'} \\ \dot{\psi}_{aa'} \end{Bmatrix} = [B(\theta_{aa'}, \psi_{aa'})] \; [AG(\phi_{ag},\theta_{ag},\psi_{ag}) \begin{Bmatrix} \omega_3^{G/N} \\ \omega_2^{G/N} \\ \omega_3^{G/N} \end{Bmatrix}$$

FOV B

$$x_{bj} = f_b \left[\frac{BN_{11} \cdot L_{1j} + BN_{12} \cdot L_{2j} + BN_{13} \cdot L_{3j}}{BN_{31} \cdot L_{1j} + BN_{32} \cdot L_{2j} + B_{33} \cdot L_{3j}}\right] + x_{pb} \qquad (3.2a)$$

$$= \text{function } (\underbrace{\phi_{an}, \theta_{an}, \psi_{an}}_{\text{orientation } \blacktriangleleft\text{'s of FOV A}}; \underbrace{\phi_{ba}, \theta_{ba}, \psi_{ba}}_{\text{interlock } \blacktriangleleft\text{'s from B to A}}; \underbrace{L_{1j}, L_{2j}, L_{3j}}_{\text{dir. cosines toward jth star}}; \underbrace{x_{pb}, f_b}_{\text{FOV B calibration constants}})$$

$$y_{bj} = f_b \left[\frac{BN_{21} \cdot L_{1j} + BN_{22} \cdot L_{2j} + BN_{23} \cdot L_{3j}}{BN_{31} \cdot L_{1j} + BN_{32} \cdot L_{2j} + BN_{33} \cdot L_{3j}}\right] + y_{pb} \qquad (3.2b)$$

$$= \text{function } (\underbrace{\phi_{an}, \theta_{an}, \psi_{an}}_{\text{orientation } \blacktriangleleft\text{'s of FOV A}}; \underbrace{\phi_{b\varepsilon}, \theta_{ba}, \psi_{b\varepsilon}}_{\text{interlock } \blacktriangleleft\text{'s from B to A}}; \underbrace{L_{1j}, L_{2j}, L_{3j}}_{\text{dir. cosines toward jth star}}; \underbrace{y_{pb}, f_b}_{\text{FOV B calibration constants}})$$

$$[BN] = [BN(\phi_{an}, \theta_{an}, \psi_{an}; \phi_{b\varepsilon}, \theta_{b\varepsilon}, \psi_{ba})] = [BA][AN]$$

$$[BA] = [BA(\phi_{ba}, \theta_{ba}, \psi_{ba})] =$$

$$= \begin{bmatrix} c\psi_{ba} & s\psi_{ba} & 0 \\ -s\psi_{ba} & c\psi_{ba} & 0 \\ 0 & 0 & 1 \end{bmatrix} \begin{bmatrix} 1 & 0 & 0 \\ 0 & c\theta_{ba} & s\theta_{ba} \\ 0 & -s\theta_{ba} & c\theta_{ba} \end{bmatrix} \begin{bmatrix} c\phi_{ba} & s\phi_{ba} & 0 \\ -s\phi_{ba} & c\phi_{ba} & 0 \\ 0 & 0 & 1 \end{bmatrix} \qquad (3.2c)$$

$\begin{Bmatrix} L_{1j} \\ L_{2j} \\ L_{3j} \end{Bmatrix}$ = direction cosines toward the jth star appearing in FOV B.

In trying to compare measured image centroid coordinates from Process A with computed image coordinates from Eqs. (3.1) and (3.2), one is immediately faced with several difficulties:

$$- \Omega[A'O(\phi_{a'o},\theta_{a'o},\psi_{a'o})] \begin{Bmatrix} c\phi_{ao}s\psi_{ao} + s\phi_{ao}s\theta_{ao}c\psi_{ao} \\ c\phi_{ao}c\psi_{ao} - s\phi_{ao}s\theta_{ao}s\psi_{ao} \\ -s\phi_{ao}c\theta_{ao} \end{Bmatrix}. \quad (2.35)$$

Like Eqs. (2.33), Eqs. (2.35) are more complex than Eqs. (2.29) or (2.30) but offer the advantages of near linearity and no singularities for the case of one vehicle rotation about $\underline{g}_2$ per orbit.

3.0 STAR PATTERN RECOGNITION/ATTITUDE DETERMINATION

3.1 Some Preliminary Remarks

Figure 3.1 displays a typical set of measured image coordinates, a simulated set of coordinates (based upon apriori angle estimates) and an uncertainty region on the celestial sphere.

The cataloged star images are projected from the celestial sphere onto the CCD image planes via the colinearity equations

FOV A

$$x_{ai} = f_a\left[\frac{AN_{11} \cdot L_{1i} + AN_{12} \cdot L_{2i} + AN_{13} \cdot L_{3i}}{AN_{31} \cdot L_{1i} + AN_{32} \cdot L_{2i} + AN_{33} \cdot L_{3i}}\right] + x_{pa} \tag{3.1a}$$

$$= \text{function}\ (\underbrace{\phi_{an}, \theta_{an}, \psi_{an}}_{\text{orientation } \measuredangle\text{'s of FOVA}};\ \underbrace{L_{1i}, L_{2i}, L_{3i}}_{\text{dir. cosines to ith star}};\ \underbrace{x_{pa}, f_a}_{\text{FOV A calibration constants}})$$

$$y_{ai} = f_a\left[\frac{AN_{21} \cdot L_{1i} + AN_{22} \cdot L_{2i} + AN_{23} \cdot L_{3i}}{AN_{31} \cdot L_{1i} + AN_{32} \cdot L_{2i} + AN_{33} \cdot L_{3i}}\right] + y_{pa} \tag{3.1b}$$

$$= \text{function}\ (\underbrace{\phi_{an}, \theta_{an}, \psi_{an}}_{\text{orientation } \measuredangle\text{'s of FOV A}};\ \underbrace{L_{1i}, L_{2i}, L_{3i}}_{\text{star dir. cosines}};\ \underbrace{y_{pa}, f_a}_{\text{FOV A calibration constants}})$$

$$[AN] = [AN(\phi_{an}, \theta_{an}, \psi_{an})] =$$

$$\begin{bmatrix} c\psi_{an} & s\psi_{an} & 0 \\ -s\psi_{an} & c\psi_{an} & 0 \\ 0 & 0 & 1 \end{bmatrix} \begin{bmatrix} c\theta_{an} & 0 & -s\theta_{an} \\ 0 & 1 & 0 \\ s\theta_{an} & 0 & c\theta_{an} \end{bmatrix} \begin{bmatrix} 1 & 0 & 0 \\ 0 & c\phi_{an} & s\phi_{an} \\ 0 & -s\phi_{an} & c\phi_{an} \end{bmatrix} \tag{3.1c}$$

$$\begin{Bmatrix} L_{1i} \\ L_{2i} \\ L_{3i} \end{Bmatrix} = \begin{Bmatrix} \cos\alpha_i & \cos\delta_i \\ \sin\alpha_i & \cos\delta_i \\ \sin\delta_i & \end{Bmatrix} = \text{direction cosines toward the ith star appearing in FOV A, referenced to the inertial axes of the mission star catalog (see appendix 1)} \tag{3.1d}$$

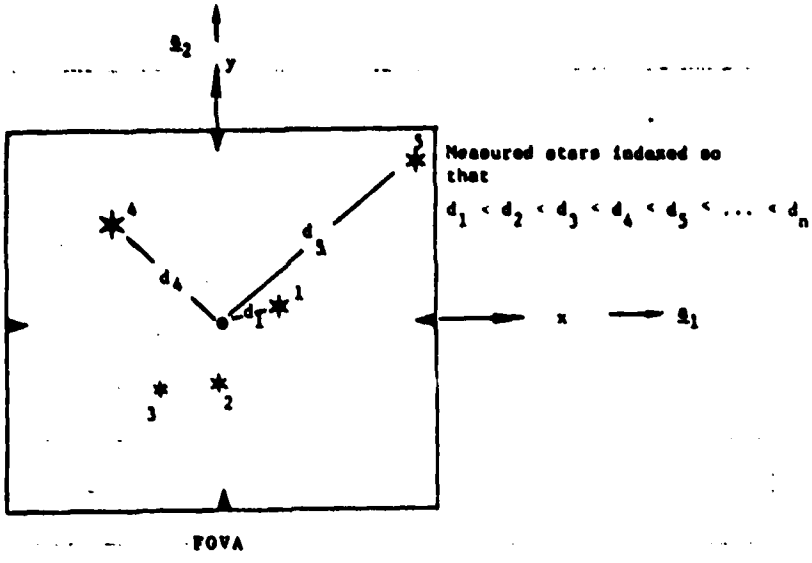

Measured stars ordered according to increasing distance from the optical boresight $[d_i = \sqrt{x_i^2 + y_i^2}]$

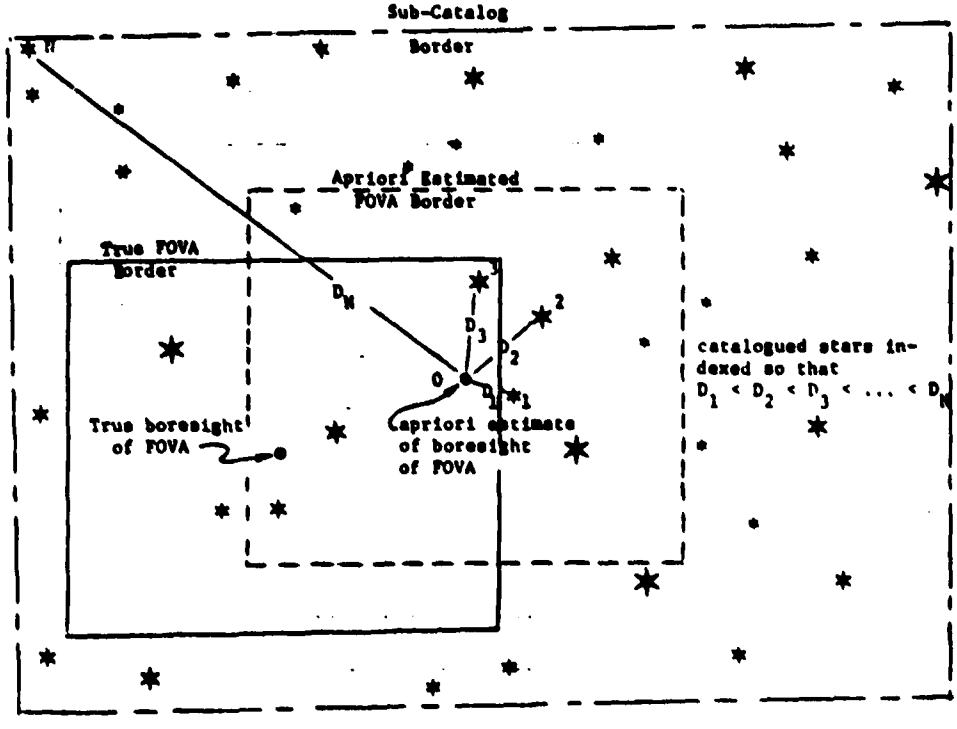

Stars in each sub-catalog are indexed according to angular distance off estimated boresight vector $[\cos D_{oi} = \cos(a_o - a_i)\cos\delta_o\cos\delta_i + \sin\delta_o\sin\delta_i]$

FIGURE 3.1 MEASURED COORDINATES, COORDINATES BASED UPON APRIORI ORIENTATION ANGLES, AND UNCERTAINTY BORDER.

(1) The orientation angles $(\phi_{an}, \theta_{an}, \psi_{an})$, in general, are not known with enough precision for the projected catalog stars to overlay measured images.

(2) The catalogued stars corresponding to measured images will not generally be known beforehand, thus, the particular star direction cosines which should be used in (3.1) and (3.2) to generate coordinates for comparison with particular measured values will not be known apriori.

One brute-force approach would involve many trial and error iterations of $(\phi_{an}, \theta_{an}, \psi_{an})$ and, for each orientation trial, one could map all stars in a particular region of the celestial sphere through Eqs. (3.1) and (3.2) and then attempt to correlate them with the measured pattern. Such an approach would be ill-advised and completely unsatisfactory in view of its inefficiency, especially for on-board computation.

The key to efficient star identification is to take advantage of the sub-ten-arc second precision of Process A; the angles between pairs of measured stars are very well determined by the measured coordinates and can be used to identify the corresponding catalogued stars. The cosine of the angle between a typical pair of measured stars can be computed from the measured image coordinates as

$$c_{ij} \equiv \cos\theta_{ij} = \frac{(x_i x_j + y_i y_j + f^2)}{\sqrt{(x_i^2 + y_i^2 + f^2)(x_j^2 + y_j^2 + f^2}} \tag{3.3}$$

The cosine of the angle between a typical pair of cataloged stars can be computed from the cataloged data as

$$C_{IJ} = \cos\theta_{IJ} = L_{1_I} L_{1_J} + L_{2_I} L_{2_J} + L_{3_I} L_{3_J}. \tag{3.4}$$

The pattern recognition logic developed below makes use of the smallness of

the difference between (3.3) and (3.4) as a means to tentatively identify the measured stars in the catalog.

The sequence of calculations and logical decisions for accomplishing the pattern matching and attitude angle estimation is not unique, but we feel an autonomous on-board algorithm should have the following features:

(1) Allow a wide variation in the quality of apriori orientation uncertainly [from say, several degrees (start up situation) to several arc seconds (steady state mode)], yet, be relatively efficient and highly reliable in each case.

(2) Allow a "reasonable" mis-match between the set of cataloged and measured stars [to reflect the realistic occurence of occasional spurious measured images, measurement of binary stars (which we have deleted from the mission catalog to avoid the problems associated with them), and uncertainties in the spectral properties of the CCD array and optical system and the cataloged information].

(3) Permit continuous re-calibration of the interlock angles between FOV A and FOV B, to compensate for the common event of significant thermal deformation cycling.

(4) Seemingly in conflict with the first three requirements, the steady-state "cycle time" (to complete the transformation from image coordinate measurements to output orientation and interlock angle measurements) should be kept small; it is felt most desirable that the cycle time be less than 30 seconds (within the constraints of on-board computation).

A macroscopic "functional logic flow" of the present Process B software (presently operational on the IBM 370/158, computer to be converted to the HP 9845 microcomputer during Phase II) is shown in Figure 3.2. This system has been implemented in FORTRAN and (on the basis of

simulations, as summarized in Section 5.0) appears to meet the first three of the above objectives quite satisfactorily. The degree to which objective (4) can be met will be studied in detail, by implementing and optimizing this software on the HP 9845S computer during Phase II.

FIGURE 3.2 PROCESS B
STAR IDENTIFICATION/DISCRETE ATTITUDE ESTIMATION
FUNCTIONAL LOGIC FLOW

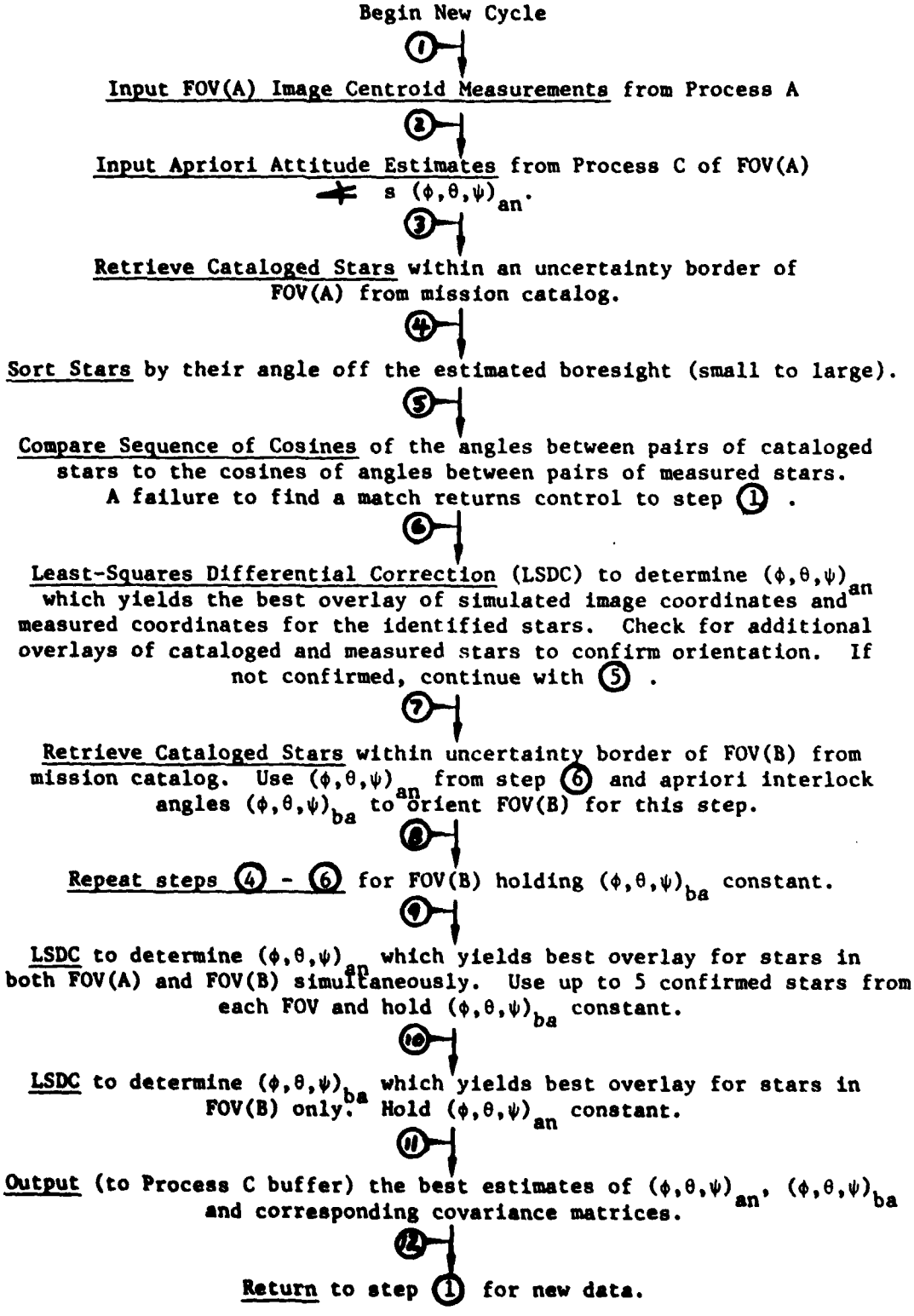

4.0 ATTITUDE PREDICTION/OPTIMAL SEQUENTIAL ATTITUDE ESTIMATION

4.1 Preliminary Comments on Definition of the State Vector

Process B, as described in section 3.0, provides discrete estimates of orientation angles (ϕ_{an}, θ_{an}, ψ_{an}) orienting FOV A in inertial space and interlock angles (ϕ_{ba}, θ_{ba}, ψ_{ba}) between FOV B and FOV A. These estimates are valid at instants which lag real time by an amount equal to the real elapsed time required to perform the computations of Process B. During this finite time interval (typically, a fraction of a minute), the gyro measurements of angular rates can be integrated to estimate vehicle orientation. Unfortunately several sources of uncertainty corrupt these data in real life applications:

> rate biases, noise, A/D conversion errors, time delays, and lack of orthogonality (gyro instrument errors)
>
> uncertain interlock angles between the gyro axes and the FOV A CCD image plane axes.

Of these error sources, the most significant are the rate biases. Fortunately, the gyro rate measurements will typically be integrated for only a fraction of a minute before receipt of heavily weighted angles from Process B, so small uncompensated gyro errors will not be reflected in a long-term degradation of precision. Any attitude estimation algorithm which ignores one or more of the above problems (for the purpose of establishing a realizable algorithm) should, however, be evaluated by establishing "truth models" in which realistic rate data can be processed by a sub-optimal Process C algorithm then comparing the estimated orientation history with the truth.

If on-board computational constraints were not present, one would probably consider developing an algorithm for estimating the relatively high dimensioned state vector

$$X^T = \{\underbrace{\phi_{an},\theta_{an},\psi_{an}}_{\text{orientation of FOV A in inertial space}};\ \underbrace{b_1,b_2,b_3}_{\text{biases in the rate measurements}};\ \underbrace{\phi_{ag},\theta_{ag},\psi_{ag}}_{\text{interlock of FOV A axes to the gyro frame}};\ \underbrace{p_1,p_2,\ldots,p_n}_{\text{orthogonality correction, time delays, other gyro error source parameters}}\} \quad (4.1)$$

Consistent with the fact that the estimation algorithm will be designed to prevent long term accumulation of rate errors and recognizing that effects of deleting all gyro parameters (except the biases) will result in most of the errors being absorbed (due to high correlation) into slightly incorrect aliased values for the rate biases (which aren't, in themselves, of crucial interest), we have adopted the six dimensional state vector

$$X^T = \{\phi_{an},\theta_{an},\psi_{an};\ b_1,b_2,b_3\} \quad (4.2)$$

Our simulations support the conclusion that setting all other gyro parameters and interlocks to nominal apriori values does not significantly degrade the Kalman filter *updates* of $(\phi_{an},\theta_{an},\psi_{an})$ although the forward propagations of motion [between Process B outputs] is degraded. For the Phase I computer software development, we have used exclusively the six element state vector of Eq. (4.2).

The angular velocity measurements are considered to be composed of three terms

$$\tilde{\omega}_i(t) = \omega_i(t) + b_i + v_i(t), \quad i = 1,2,3 \quad (4.3)$$

$\tilde{\omega}_i(t)$	$\omega_i(t)$	b_i	$v_i(t)$
measured, A/D converted rate	true angular rate	constant bias	noise

The raw signal $\tilde{\omega}_i(t)$* are integrated numerically into angular motion by solving the kinematical differential equations

$$\begin{Bmatrix} \dot{\phi}_{an} \\ \dot{\theta}_{an} \\ \dot{\psi}_{an} \end{Bmatrix} = \frac{1}{\cos\theta_{an}} \begin{bmatrix} \cos\psi_{an} & -\sin\psi_{an} & 0 \\ \sin\psi_{an}\cos\theta_{an} & \cos\psi_{an}\cos\theta_{an} & 0 \\ -\cos\psi_{an}\sin\theta_{an} & \sin\psi_{an}\sin\theta_{an} & \cos\theta_{an} \end{bmatrix} [AG(\phi_{ag},\theta_{ag},\psi_{ag})] \begin{Bmatrix} \tilde{\omega}_1 - b_1 \\ \tilde{\omega}_2 - b_2 \\ \tilde{\omega}_3 - b_3 \end{Bmatrix} \quad (4.4)^{**}$$

using 4-cycle Runge-Kutta. The equations (4.4) are exact kinematical relationships, errors in $[\phi_{an}(t), \theta_{an}(t), \psi_{an}(t)]$ can result only from one of the following sources

(a) initial condition errors

(b) errors in $(\phi_{ag},\theta_{ag},\psi_{ag})$ estimates

(c) errors in $\tilde{\omega}_i$

(d) truncation and arithmetic errors in the numerical integration process.

Error sources (b) and (c) are correlated and correctable (in the Kalman filter algorithm), errors (d) are not a significant practical difficulty in the present case except near the geometric singularity $[|\theta_{an}| = 90°]$ of the 1-2-3 Euler angle sequence, and since the initial conditions are the $\leq$ 5 arc second error output of Process B, the errors (a) are not damaging over short time intervals.

---

*The solutions for $[\phi_{an}(t),\theta_{an}(t),\psi_{an}(t)]$ are significantly improved by judicious presmoothing of $\tilde{\omega}_i(t)$, but the degree of improvement is not dramatic over relatively short integration intervals. We have found that integrating "raw" rate data (corrected only for biases) by four cycle Runge-Kutta produces satisfactory results for the present application (assuming about 1 $\widehat{\text{sec.}}$/sec. noise for the gyro angular velocity measurements).

**We have considered several other angular state variables and associated kinematics (see section 2.0). During Phase II, we will conduct sufficient studies on the HP 9845S to allow a final selection to be made. Our simulations to date have considered primarily the above case.

4.2 The State Differential Equations

STATE VECTOR:

$$X = \begin{Bmatrix} x_1 \\ x_2 \\ x_3 \\ x_4 \\ x_5 \\ x_6 \end{Bmatrix} = \begin{Bmatrix} \phi_{an} \\ \theta_{an} \\ \psi_{an} \\ b_1 \\ b_2 \\ b_3 \end{Bmatrix} \tag{4.5}$$

OBSERVATION VECTOR:

$$Y = \begin{Bmatrix} \phi_{an} \\ \theta_{an} \\ \psi_{an} \end{Bmatrix} \text{ ("observations" are the discrete output of Process B)} \tag{4.6}$$

DIFFERENTIAL EQUATIONS:

$$\begin{Bmatrix} \dot{x}_1 \\ \dot{x}_2 \\ \dot{x}_3 \end{Bmatrix} = \frac{1}{cx_2} \begin{pmatrix} cx_3 & -sx_3 & 0 \\ sx_3cx_2 & cx_3cx_2 & 0 \\ -cx_3sx_2 & sx_3sx_2 & cx_2 \end{pmatrix} [AG] \begin{Bmatrix} \tilde{\omega}_1 - b_1 \\ \tilde{\omega}_2 - b_2 \\ \tilde{\omega}_3 - b_3 \end{Bmatrix} \tag{4.7a}$$

$$\begin{aligned} \dot{x}_4 &= 0 \\ \dot{x}_5 &= 0 \\ \dot{x}_6 &= 0 \end{aligned} \tag{4.7b}$$

STATE TRANSITION MATRIX:

$$\Phi(t,t_k) = \left[\frac{\partial[\phi_{an}(t),\theta_{an}(t),\psi_{an}(t),b_1,b_2,b_3]}{\partial[\phi_{an}(t_k),\theta_{an}(t_k),\psi_{an}(t_k),b_1,b_2,b_3]} \right]$$

or

$$\Phi(t,t_k) = \left[\begin{array}{ccc|ccc} & \Phi_{11} & & & \Phi_{12} & \\ \hline 0 & 0 & 0 & 1 & 0 & 0 \\ 0 & 0 & 0 & 0 & 1 & 0 \\ 0 & 0 & 0 & 0 & 0 & 1 \end{array}\right] \tag{4.8a}$$

where

$$\Phi_{11}(t,t_k) = \frac{\partial[\phi_{an}(t),\theta_{an}(t),\psi_{an}(t)]}{\partial[\phi_{an}(t_k),\theta_{an}(t_k),\psi_{an}(t_k)]} \tag{4.8b}$$

$$\Phi_{12}(t,t_k) = \frac{\partial[\phi_{an}(t),\theta_{an}(t),\psi_{an}(t)]}{\partial[b_1,b_2,b_3]} \tag{4.8c}$$

The two nontrivial submatrices of partial derivatives are obtained by solving the two differential equations

$$\frac{d}{dt}[\Phi_{11}(t,t_k)] = [F(t)]\ [\Phi_{11}(t,t_k)] \tag{4.8d}$$

$$\frac{d}{dt}[\Phi_{12}(t,t_k)] = \frac{-1}{cx_2}\begin{bmatrix} cx_3 & -sx_3 & 0 \\ sx_3cx_2 & cx_3cx_2 & 0 \\ -cx_3sx_2 & sx_2sx_2 & cx_2 \end{bmatrix}[AG] + [F(t)]\ [\Phi_{12}t,t_k)] \tag{4.8e}$$

with initial conditions $[\Phi_{11}(t_k,t_k)] = [1]$, $[\Phi_{12}(t_k,t_k)] = [0]$,

and where

$$[F(t)] = \left[\frac{\partial(\dot{x}_1,\dot{x}_2,\dot{x}_3)}{\partial(x_1,x_2,x_3)}\right], \tag{4.8f}$$

and the columns of $[F(t)]$ are given by the following equations

$$[F(t)] = [F_\phi\ F_\theta\ F_\psi] \tag{4.8g}$$

$$\{F_\phi\} = \begin{Bmatrix} \frac{\partial\dot{\phi}}{\partial\phi} \\ \frac{\partial\dot{\theta}}{\partial\phi} \\ \frac{\partial\dot{\psi}}{\partial\phi} \end{Bmatrix} \begin{Bmatrix} \frac{\partial\dot{x}_1}{\partial x_1} \\ \frac{\partial\dot{x}_2}{\partial x_1} \\ \frac{\partial\dot{x}_3}{\partial x_1} \end{Bmatrix} - \begin{Bmatrix} 0 \\ 0 \\ 0 \end{Bmatrix}, \begin{matrix} \phi & \phi_{an} \\ \theta & \theta_{an} \\ \psi & \psi_{an} \end{matrix} \tag{4.8h}$$

$$\{F_\theta\} = \begin{Bmatrix} \frac{\partial\dot{\phi}}{\partial\theta} \\ \frac{\partial\dot{\theta}}{\partial\theta} \\ \frac{\partial\dot{\psi}}{\partial\theta} \end{Bmatrix} \begin{Bmatrix} \frac{\partial\dot{x}_1}{\partial x_2} \\ \frac{\partial\dot{x}_2}{\partial x_2} \\ \frac{\partial\dot{x}_3}{\partial x_2} \end{Bmatrix}$$

$$\{F_\theta\} = \frac{sx_2}{c^2x_2}\begin{bmatrix} cx_3 & -sx_3 & 0 \\ sx_3cx_2 & cx_3cx_2 & 0 \\ -cx_3sx_2 & sx_3sx_2 & cx_2 \end{bmatrix}\begin{Bmatrix} \omega_1 - b_1 \\ \omega_2 - b_2 \\ \omega_3 - b_3 \end{Bmatrix}$$

$$+ \frac{1}{c\theta}\begin{bmatrix} 0 & 0 & 0 \\ -sx_3sx_2 & -cx_3sx_2 & 0 \\ -cx_3cx_2 & sx_3cx_2 & -sx_2 \end{bmatrix}\begin{Bmatrix} \omega_1 - b_1 \\ \omega_2 - b_2 \\ \omega_3 - b_3 \end{Bmatrix} \qquad (4.8i)$$

$$\{F_\psi\} = \begin{Bmatrix} \frac{\partial\dot{\psi}}{\partial\psi} \\ \frac{\partial\dot{\theta}}{\partial\psi} \\ \frac{\partial\dot{\psi}}{\partial\psi} \end{Bmatrix} - \begin{Bmatrix} \frac{\partial\dot{x}_1}{\partial x_3} \\ \frac{\partial\dot{x}_2}{\partial x_3} \\ \frac{\partial\dot{x}_3}{\partial x_3} \end{Bmatrix}$$

$$\{F_\psi\} = \frac{1}{cx_2}\begin{pmatrix} -sx_3 & -cx_3 & 0 \\ cx_3cx_2 & -sx_3cx_2 & 0 \\ sx_3sx_2 & cx_3sx_2 & 0 \end{pmatrix}\begin{Bmatrix} \omega_1 - b_1 \\ \omega_2 - b_2 \\ \omega_3 - b_3 \end{Bmatrix} \qquad (3.8j)$$

The indicated partials in (4.8f) were explicitely taken by differentiating equation (4.7a).

4.3 The Kalman Estimation Algorithm

The classical extended Kalman filter equations (see ref. 4) in the form

STATE UPDATE RECURSION

$$\hat{X}_{k+1}(k+1) = \bar{X}_k(k+1) + K(k+1)\{\hat{Y}(k+1) - \bar{Y}(k+1)\} \qquad (4.9)$$

COVARIANCE AND KALMAN GAIN UPDATE RECURSIONS

$$P_k(k+1) = \Phi(k+1,k)\, P_k(k)\Phi^T(k+1,k) + Q(k) \tag{4.10}$$

$$K(k+1) = P_k(k+1)H^T(k+1)[\Lambda_{v_{k+1}v_{k+1}} + H(k+1)P_k(k+1)H^T(k+1)]^{-1} \tag{4.11}$$

$$P_{k+1}(k+1) = [I - K(k+1)H(k+1)]P_k(k+1) \tag{4.12}$$

$$H(k+1) = \frac{\partial Y}{\partial X}\Big|_{\bar{X}_k(k+1)} = \begin{bmatrix} 1 & 0 & 0 & 0 & 0 & 0 \\ 0 & 1 & 0 & 0 & 0 & 0 \\ 0 & 0 & 1 & 0 & 0 & 0 \end{bmatrix} \tag{4.13}$$

Forward propagated (apriori estimates)

$$\bar{X}_k(k+1) = X \text{ at time } t_{k+1} \text{ based upon k data subsets} \tag{4.14}$$

= forward Runge-Kutta integration equations in sec. 4.2 of the previous estimate $\hat{X}_k(k)$.

$$\bar{Y}(k+1) = \begin{Bmatrix} \phi(t_{k+1}) \\ \theta(t_{k+1}) \\ \psi(t_{k+1}) \end{Bmatrix} = \text{first three elements of } \bar{X}_k(t_{k+1}) \tag{4.15}$$

COVARIANCE/PROCESS NOISE MATRICES

$\Lambda_{v_{k+1}v_{k+1}}$ = 3x3 covariance matrix of errors associated with $Y^T = (\phi_{an}, \theta_{an}, \psi_{an})$, from Process B output.

$Q(t)$ = Process noise, to reflect uncertainty in $(\phi_{an}, \theta_{an}, \psi_{an})$ arising due to errors in the rate gyros.

Our simulations indicate that angular rate errors (with Gaussian white noise and variance of σ_{GYRO}^2) result in the following process noise matrix

$$Q = \begin{pmatrix} 1 & 0 & 0 \\ 0 & 1 & 0 \\ 0 & 0 & 1 \end{pmatrix} \sigma_{GYRO}^2 \, (t - t_k) \tag{4.16}$$

4.4 Some observations

The above algorithm is not put forth as the optimal, final word on the subject. However, the simulations of section 5 support the conclusion that it is (in most respects) entirely satisfactory. The primary shortcoming

is the presence of twice per orbit singularities in the 1-2-3 angles (ϕ_{an},θ_{an},ψ_{an}). As is discussed in section 2, this difficulty can be readily overcome in a number of ways; the best way to overcome this relatively minor problem will be established during Phase II.

5.0 SIMULATIONS

In order to test the logic and algorithms for all three processes, it is necessary to generate "truth models" to which simulations can be compared. These truth models must accurately represent the behavior of the instrument with the capability to simulate "perfect" data as well as data with realistic (but known) error sources.

5.1 Process A Simulations

For Process A, we assume that the star images from the star sensors results from "centroiding" of star energy images by a 70 mm focal length lens onto a CCD array, displaced slightly behind the image plane (2.425 mm) to allow for image defocus. Since the image plane size is small compared to the focal length, we do not include any image plane distortions (although this assumption can be readily modified for specific applications). Presumably, if there are distortions in the final instrument, their effect will be small and assumed constant in time and, thus, will be correctable by appropriate apriori calibrations and included in the software for Process A. We assume that the true stellar image coordinates are given by the stellar colinearity equations (see Sec. 3.1).

For Process A simulations, we used typical CCD parameters for dark current, sensitivity and size. Assuming that a defocused star image illuminates a 4 x 4 submatrix of pixels, we interpolated the response to determine the image centroid. The number of test cases was not large but gave us confidence that the centroid could routinely be found with an accuracy to about 0.1 pixel. For a pixel size of ~0.030 mm, we assumed that the standard deviation of image errors is σ~0.0034 mm (.0034 mm corresponds to ~10 arcseconds with a 70 mm focal length lens). See Appendix 2 for additional information on parameters assumed for the CCD. On the basis

of these tests, Process A output is simulated by computing true image coordinates and perturbing them slightly with simulated centroiding/ measurement errors (Gaussian random numbers) of standard deviation .0034 mm.

5.2 Process B Simulations

The simulations of Process B consisted of determining the accuracy to which Process B software recovered the vehicle orientation from a wide variety of simulated star measurements from Process A. As examples, we summarize ten cases in the following discussion. The true orientations were selected at random and true stellar image coordinates of up to 10 stars per field of view were perturbed by Gaussian measurement noise and used as input to Process B. The initial angle estimates for vehicle orientation were displaced 1° from the truth in each angle. With this initial estimate, the first cataloged pair (after sorting) was usually matched with the correct stored measured pair. Typically, 4-5 least-squares iterations were required to bring the image coordinates of the first identified star pair into agreement with the measured star pair coordinates. Once this was done, there was usually no difficulty in finding additional stars to confirm the match (i.e., the orientation determined by a correctly identified star pair usually causes other projected images to nearly overlay the corresponding measured images). In several cases there were fewer than expected confirmations. This occurs when one has a particularly large error sample on either the first identified star pair or on the remaining stars.

Often, the particular noise sample for image displacements can impart a significant rotation of the FOV about the boresight. This was not a problem in the combined solution, however, since the angle around the boresight is determined accurately by having the two FOV 90° apart.

However, in solving for the final interlock angles, the rotation about the boresight for FOV(B) is often very poorly determined due to this noise/geometric effect. Since one least- squares reduction.does not reliably recover the interlock angles to the desired precision, it is necessary to average over back least-squares estimates of the three interlocks in order to smooth out these variations and monitor the true variations of interlock angles. This averaging is justified over up to 15 minutes of real time, since any real variations of interlocks will be associated with an orbit period (thermal cycling).

Table 5-1 lists data for the 10 simulation trials. For each trial, the number of stars used in the least squares correction is given. Five stars is the current maximum number used in the least-squares correction per FOV. Data for four correction stages are give: 1) solution of FOV(A), 2) solution of FOV(B), 3) combined solution using FOV(A) and FOV(B), and 4) adjustment of interlocks for FOV(B). The deviations given are deviations from the truth in arcseconds. As mentioned earlier, the rotation about the boresight is the most poorly determined angle (ψ_{an} in stage 1 and ψ_{ba} in stage 4). The interlock values given are single least-squares reductions; these errors are reduced in practice, proportional to the square root of the number of back estimates averaged. Note that in nearly all combined solutions the deviation from the true vehicle orientation is < 10 arcseconds. Note the very poor results for example 4. The inacuracies here are due primarily to the fact that θ_{an} ~ 91°--near the singularity for the 1-2-3 Euler angle sequence used for the Process B algorithm. This should not cause any long term problems since the vehicle will soon rotate to new orientations. Also in practice, one will introduce the "orbiting frame" so that the "ao" angles will be estimated; for this case, one would generally be estimating small 1-2-3 angles (which will not encounter the poor geometry of example 4).

Table 5-1. Process B Simulation Examples

Case #	No. of Stars used in solution FOV(A)	FOV(B)	"AN" Vehicle orientation angles Δφ (arcsec)	Δθ	Δψ	"BA" Interlock angles (single estimate) Δφ (arcsec)	Δθ	Δψ
1	5		-2.7	2.1	-50.3			
		5	-168.9	179.4	100.6			
	5	5	-0.6	0.0	0.2			
		5				-5.4	-1.2	-22.6
2	5		-14.0	9.5	254.3			
		3	85.0	-21.4	-44.6			
	5	3	-5.8	3.3	-2.5			
		3				0.8	-1.2	83.3
3	5		11.8	0.4	306.1			
		5	0.8	-1.0	5.0			
	5	5	3.5	-0.6	2.9			
		5				0.8	-1.2	-0.8
4	4		154.7	-5.0	-208.7			
		3	-5375.3	-159.6	283.0			
	4	3	92.8	-2.9	-93.2			
		3				5.0	11.1	188.5
5	5		-1.6	-1.2	96.7			
		5	31.4	-120.9	-25.0			
	5	5	0.4	-3.3	-2.3			
		5				1.2	-3.3	120.4
6	5		-6.6	-1.0	91.4			
		5	-85.0	153.7	-59.2			
	5	5	1.6	3.1	-1.4			
		5				1.2	-7.4	163.8
7	4		9.3	5.0	157.2			
		5	-1.0	-29.9	4.5			
	4	5	3.1	2.9	2.5			
		5				-0.8	7.0	-32.2
8	5		0.4	2.5	56.5			
		5	7.6	2.5	5.0			
	5	5	3.7	0.4	5.0			
		5				-0.8	2.9	2.9
9	4		6.6	4.7	28.5			
		5	23.1	19.2	-17.9			
	4	5	8.7	4.1	-7.8			
		5				1.2	0.8	-17.7
10	5		-15.5	-2.1	229.8			
		5	-44.3	-20.6	17.3			
	5	5	-5.2	0.0	11.1			
		5				-0.8	-3.3	-42.5

5.3 Process C Simulations

The primary function of Process C that must be tested is the Kalman filter algorithm. That is, we must determine how well the filter recovers the biases and updates the optimal vehicle orientation. To test this, we computed and saved the "true" state, consisting of three orientation angles for 20 one minute intervals. The motion history is given by the rotation around the vehicle "2" axis with a rate of one rotation every 1.5 hour plus a low amplitude sinusoid:

$$\omega_t = \omega_o(1 + .1 \sin((t - t_o)\omega_o)).$$

The rotation about the other two axes is nominally zero. We consider two cases:

$$(\phi,\theta,\psi)_{an_{(t=0)}} = (0°, 0°, 0°) \text{ and } (\phi,\theta,\psi)_{an_{(t=0)}} = (0°, 91°, 0°).$$

For the simulations we start with the initial state estimate displaced 1° from the truth in all angles and biases set to zero. Process B output for each interval, consisting of three discrete angles, is simulated by perturbing the true orientation angles by Gaussian noise having a standard deviation of five arcseconds [(note, we do not yet have Process B and C implemented in parallel)]. A 3 x 3 observation covariance matrix associated with the three orientation angles is consistently defined using the same standard deviation. The true angular rates are computed each time angular rates are needed by the Runge-Kutta integration and the fixed biases plus a random measurement noise was added to all three rates. For simplicity, we use identical "true" bias values for all three rate simulations. The random noise added to the rates was uncorrelated white noise with a standard deviation of one arcsecond per second. The estimated biases from previous Kalman filter updates are subtracted from the simulated gyro rates described above in each integration of the kinematic equations.

Figures 5-1 and 5-2 show the results of two simulations typical of those discussed above. Plotted in each figure is the total deviation $\Delta\Psi = (\Delta\phi^2 + \Delta\theta^2 + \Delta\psi^2)^{1/2}$ of the integrated state and the filtered state from the true orientation and the estimated standard deviation of $\Delta\Psi$ (from the updated covariance matrix of the Kalman filter). The first several integrated states lie off the scale in both figures because of the inaccurate initial state estimate (primarily the very poor bias estimates). Note that after the second and third state updates, respectively, that the biases are recovered sufficiently well that each new integrated state is displaced less than 30 arcseconds from the true orientation. Another important point to note is that the optimal state estimate for the orientation nearly equals the Process B orientation. This is because the process B angles have a much higher weight, in general, than the forward integrated angles from the Runge-Kutta integration of the noise-corrupted gyro data. In fact, on the scale of the plots of Fig. 5-1 and 5-2 the optimal state is nearly indistinguishable from the Process B output state.

These figures demonstrate that the Kalman filter formulation, in its present form, should provide sufficiently good estimates for the next Process B cycle. However, examination of the recovered biases given by the optimal estimate shows that the sequence of estimates have a large scatter about the true value, although the average value of each bias, over time, is very near to the true value. This is due primarily to the similarity in magnitude between the baises and the unfiltered gyro measurement noise. The effect of the poorly determined biases is to make the next integrated state deviate more from the truth than would be the case with more precise bias values. As mentioned above, all steady state deviations are less than 30 arcseconds, which is sufficiently accurate for re-initiating Process B. For some applications, however, it may be

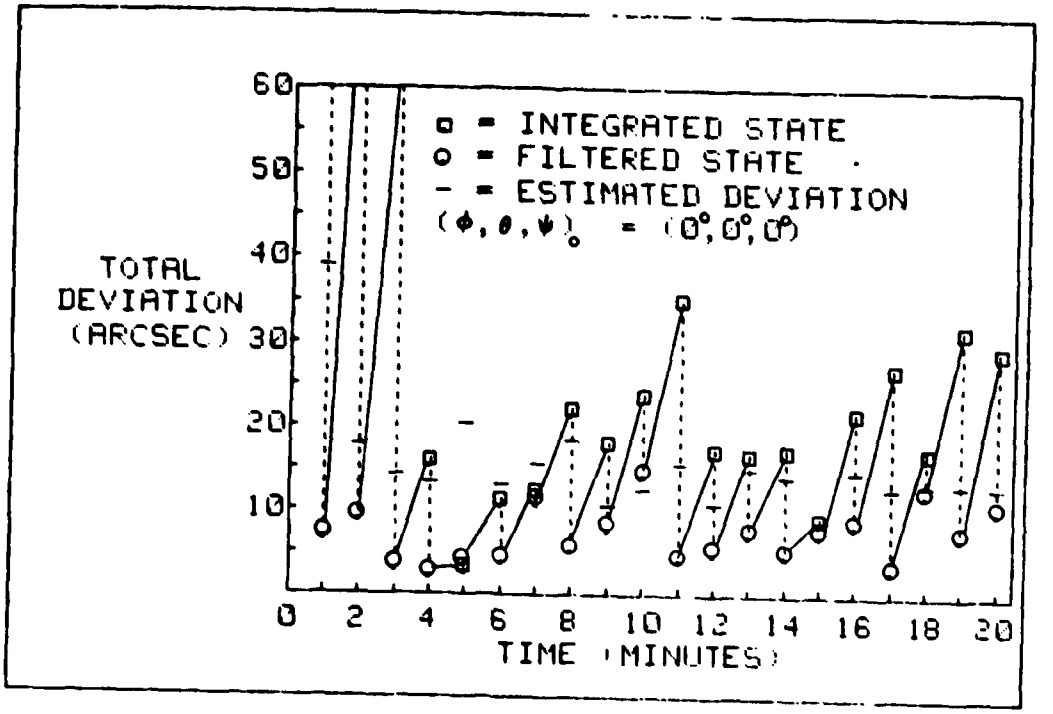

Figure 5.1. Kalman filter results for Process C simulation: Case I

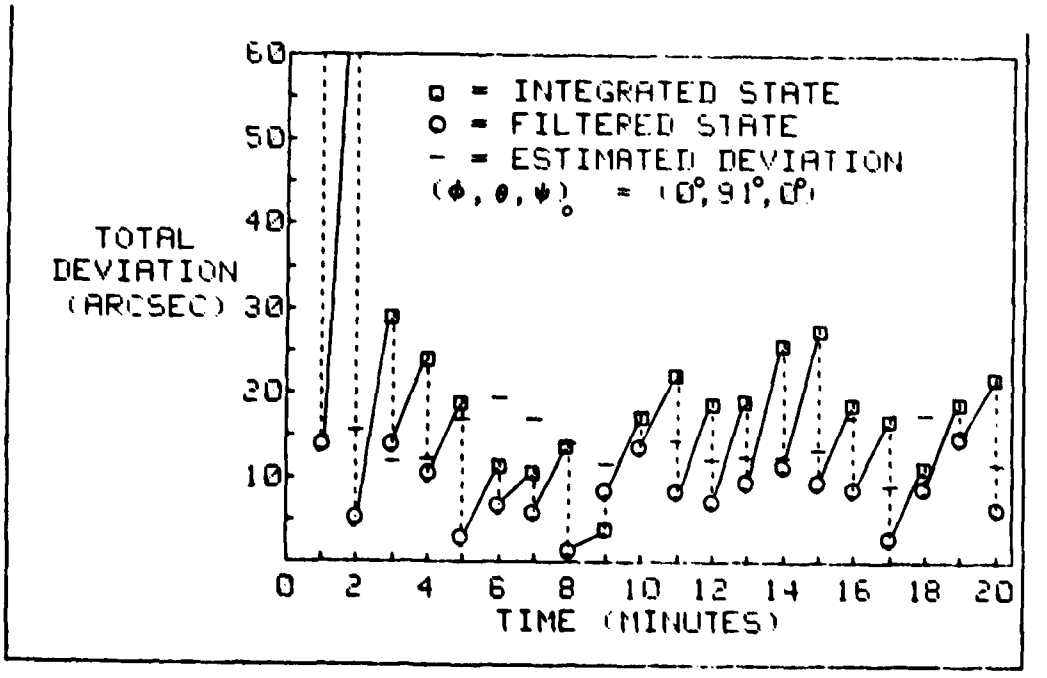

Figure 5.2. Kalman filter results for Process C simulation: Case II

desirable to achieve higher precision. In these cases, we suggest either one, or both, of two simple techniques to reduce errors due to gyro errors. The first, and perhaps simplest, is to average the new bias values with several from previous Kalman filter solutions and use the averages for the next forward integration. Since the biases are assumed constant, or at least slowly varying, this averaging should not introduce significant error on the time scale of tens of minutes. The second method is to pre-filter the noisy gyro rate data to smooth out the worst of the gyro noise. Typically, many gyro measurements should become available during each Process B and C cycle (>10 readings per second). These rates could be averaged mathematically or filtered electronically before being used by the Runge-Kutta integration package. Although these techniques will reduce the error, the integrated state will still be in error due to the errors in Process B angles and thus, in the optimal state which is used as the initial state for the next integration. The selection of any process to reduce the integrated rate errors must take into consideration not only its effectiveness, but also its cost (mainly, elapsed time), when introducing the algorithm into Process C. Significant time delays introduced may prove more harmful (in a real-time-mode) than the beneficial effects of better angular rate knowledge between Process B outputs. We will address this issue during Phase II.

6.0 CONCLUDING REMARKS AND OUTLOOK FOR PHASES II AND III

The following major results have been achieved during the Phase I effort:

A. A parallel process approach to the real-time spacecraft attitude estimation problem has been defined.

B. Preliminary FORTRAN software has been developed for:

1) Process B (star identification/spacecraft attitude estimation)

2) Process C (sequential estimation/motion integration)

Simulations with these algorithms support the validity of the basic concepts.

C. Conversion of the FORTRAN software to run in a microcomputer system (the HP 9845S) has been initiated, the preliminary indications are most favorable; it appears that the cycle time for Process C (to process orientation angle estimates and integrate rate gyro data to angle estimates for 60 real-time-seconds) is about 10 seconds. Thus Process C is presently running about 6 times as fast as real time, using a BASIC interpreter - an assembly language and optimized version of this code will run significantly faster. Thus, there is basis for optimism that the real-time attitude estimation objectives can be achieved, pending similar results for the (much more elaborate) algorithms of Process B.

During Phase II, the following major tasks will be addressed:

A. Development of refined logic and algorithms for star identification and attitude determination; the emphasis being to reduce the probability of false identification to a practically impossible event (make the probability less than 10^{-5}!) and, at the

same time, optimize the algorithms to facilitate implementation on the HP 9845S (which will be accomplished during Phase II).

B. Development of improved algorithms for Process C:

(1) Eliminate geometric singularities by re-formulating the Kalman filter in terms of Euler parameters.

(2) Studies on various pre-processors for smoothing the rate gyro data under the constraints of near-real-time, on-board calculations.

C. In preparation for interfacing Processes B and C in parallel microcomputers during Phase III, extensive timing studies and error analyses will be conducted to assess the performance of the sub-systems in the presence of large *apriori* uncertainties, spurious images, and sharp attitude maneuvers. For example, if Process B can be made to cycle several times per minute (in the steady state), then it may be possible to simplify the Process C algorithms without degrading the overall system performance (since the rate data need be integrated only for a few seconds, sophisticated pre-smoothing may eliminate insignificant errors and thereby serve only to slow down Process C's cycle time).

D. Study of the evolving CCD and related sensor technology to re-evaluate and refine the sensor models and error assumptions implicit in this research.

During Phase III, Processes B and C will be implemented in parallel, intermittently communicating microcomputers and will employ a "driver" simulation of Process A to input simulated image centroids, magnitudes and times. A "truth model" will be developed and employed to evaluate

7.0 REFERENCES

1.0 Junkins, J. L., C. C. White, and J. D. Turner, "Star Pattern Recognition for Real Time Attitude Determination", Journal of the Astronautical Sciences, Vol. XXV, No. 3, Sept. 1977.

2.0 Saloman, P. M., and W. C. Goss, "A Micro-Processor-Controlled CCD Star Tracker", AIAA Paper No. 76-116, AIAA 14th Aerospace Sciences Meeting, Washington, D.C., Jan. 1976.

3.0 Gutshall, R. L., Private Communications on the BBRC DIGISTAR CCD Star Tracker, Ball Brothers Research Corporation, Boulder, Colorado, August, 1977.

4.0 Junkins, J. L., Optimal Estimation of Dynamical Systems, Sijthoff-Noordhoff International Publishers, The Netherlands, ch. 5, 1978.

5.0 Gottlieb, D. M. "SKYMAP System Description: Star Catalog Data Base Generation and Utilization", Computer Sciences Corporation, Report CSC/SD-76/6041, Nov. 1976, Silver Springs, MD.

6.0 Charged Coupled Devices: Technology and Applications, ed. Roger Melen and Dennis Buss, New York: IEEE Press, 1977.

7.0 Johnson, H. L., "Astronomical Measurements in the Infrared", Ann. Rev. Astronomy and Astrophysics, V. 4, 193, (1966).

the systems performance. The entire system can then be studied and optimized in a realistic fashion. The objective being, of course, to gain the insights necessary to design a truly autonomous and highly reliable "attitude navigation" system. A significant by-product of this research program will be a set of well-tested and optimized algorithms which serve to automate ground-based star pattern recognition and estimation of spacecraft orientation history (from star sensor and rate gyro measurements).

APPENDIX 1

STAR DATA BASE AND MISSION CATALOG CREATION

The star catalog data base system SKYMAP (Ref. 5) has been selected as the master star data base. The SKYMAP catalog was developed from the SAO catalog and other sources specifically for attitude determination programs by NASA-GSFC. It is complete to the eighth magnitude in either the blue (B) or visual (V) magnitudes. Additionally, the catalog contains right ascensions, declinations, and, when known, the spectral type, luminosity class, and amount of interstellar absorption in the V wavelength range.

The on-board (or mission) star catalog is divided into celestial sphere cells so as to permit efficient microcomputer access during the pattern recognition process. In order to keep storage requirements for the mission catalog to a minimum, the cells do not overlap. The placement of the cell centers is given by the polar angle θ and longitude λ according to

$$\theta_n = \cos^{-1}(\xi_n) \qquad n = 0,1,2...N \tag{1.1}$$

and

$$\lambda_{nj} = \frac{2\pi j}{2n+1} \qquad j = 0,1,2,...2n \tag{1.2}$$

$$\xi_n = (-1)^n \cos\left(\frac{n\pi}{2n+1}\right), \quad n = 0,1,2...N \tag{1.3}$$

These formulae yield $(N+1)^2$ points: N+1 polar angles or declination zones with spacing $2\pi/(2N+1)$, and (2n+1) equally spaced regions in each zone.

The choice of N is somewhat arbitrary. A large N yields small cells which would require more than one cell to be accessed; a small N yields large cells which would increase the number of trials in the pattern recognition process as well as causing a possible storage problem. Taking

into account the 7° x 9° field-of-view, a value of N = 15 was chosen, yielding 256 cells of 11.6° x 11.6° or larger.

To facilitate computer access, the cells are ordered within memory according to a parameter n^2+j; a table lists the starting relative address of each cell and the number of stars in each. Thus, given a boresight estimate (θ,λ), the primary cell location is given by

$$\begin{aligned} n &= 2[\theta/\Delta\theta + 0.5] \qquad (\theta<90°) \\ &= 2N + 1 - 2[\theta/\Delta\theta + 0.5] \quad (\theta>90°) \end{aligned} \tag{1.4}$$

$$j = [\lambda/\Delta\lambda + 0.5], \tag{1.5}$$

where [x] indicates integer arithmetic (truncation to next smallest integer). The table of cells is then consulted for identification of the appropriate memory location. If the estimated boresight is near a cell boundary and/or possesses a large uncertainty, one or more neighboring cells are accessed.

The CCD is assumed (see Appendix 2) to respond to stars of I magnitude 5 or lower ~ approximately 5400 stars. If these 5400 stars are assumed to be distributed uniformly over the celestial sphere, the star density ρ would be

$$\begin{aligned} \rho &= \frac{\text{5400 stars/sphere}}{\text{41,253 square degrees/sphere}} \\ &\triangleq \text{0.13 stars/square degree} \end{aligned} \tag{1.6}$$

For a field-of-view of 7° x 9° ≙ 63 square degrees, we would expect

(63 square degrees) (0.13 stars/square degree) ≙ 8.2 stars*

in a field-of-view (assuming uniform density). To obtain a measure of the range of the number of stars actually detectable per field-of-view, the boresight was randomly oriented over the entire celestial sphere 100 times. For each trial, the mission catalog was consulted and the number

---

*Due to non-uniform star population of the celestial sphere, this number decreases to about 5 at the north galactic pole.

of stars in the field-of-view recorded. The average number of stars per field-of-view was six; in no case were fewer than two stars in the field-of-view.

APPENDIX 2

CCD Instrument Response Approximations

As mentioned in Section 1, the outputs of Process A are the interpolated centroids and instrument magnitudes for each valid star image. The purpose of this Appendix is the discussion of the approximate techniques utilized in the synthesis of these two outputs.

2.1 The Star Centroids

The centroid location (x_c, y_c) is given by

$$x_c = \frac{\Sigma_i (x_i \Sigma_j R_{ij})}{\Sigma_j \Sigma_i R_{ij}} \tag{2.1}$$

and

$$y_c = \frac{\Sigma_j (y_j \Sigma_i R_{ij})}{\Sigma_j \Sigma_i R_{ij}} , \tag{2.2}$$

where R_{ij} is the A/D converted response level of the pixel located at (x_i, y_i) and the summations are over the square array of pixels illuminated by the defocused star image (16 or 25 pixels).

Typical cell size for a CCD is approximately 0.030 mm on a side. A CCD placed behind a 70 mm focal length lens (proposed for one CCD star-sensor) gives a resolution of approximately 1.5 arc-minutes for a focused image. When spread over a 4 x 4 or 5 x 5 cell pattern, the resolution with which the centroid can be located has been found to be about 6 arc-sec. For double stars, Process A would produce image coordinates for a single star but with poorly determined image coordinates (a weighted mean of the two stars).

Detections of double stars should not be used in Process B since they would result in poor orientations. One solution to this problem is to delete from the mission catalog all star pairs with separations less

than some tolerance (~6 arc-min. in this case). There are sufficient stars in the catalog that this deletion should not seriously degrade performance. Some additional time in Process B will be used trying unsuccessfully to pair measured double stars with catalog stars, but since detection of double stars will be a relatively rare event, this time penalty should not be a significant practical problem.

2.2 CCD Magnitude Response

2.2.1 Magnitude Conversion

Due to both the different spectral qualities of various stars and the peculiarities in the unfiltered CCD response (the primary sensitivity is to red or near intra-red radiation) two stars of the same visual (V) magnitude (for example) may cause different CCD response. Hence none of the cataloged star magnitudes may be used directly. Rather, the magnitudes of the stars must be properly transformed (using the spectral properties contained in the master star catalog SKYMAP) prior to insertion in the mission catalog. Simply stated, the mission catalog must contain an "instrument magnitude" for each star.

It has been decided to convert the V magnitudes of SKYMAP to I magnitudes and utilize an I filter placed over the CCD array. The following points support this decision:

(1) Given the information in SKYMAP, one could, in principle, perform a magnitude conversion from V to a CCD magnitude. However, this would require the choice of a particular CCD detector in order to determine its response characteristics in the laboratory.

(2) The response functions of typical CCD's are quite broad, a fact which makes a rigorous conversion to a CCD magnitude

difficult in light of the complicated stellar spectral features in the blue wavelength region. A detailed description of the spectra would be requied. The I filter, on the other hand, is confined to the red wavelengths where the star spectra are relatively smooth.

(3) The I filter response peak is near that of typical CCD's. In addition, it overlaps the main peaks of the commonly accepted "typical CCD response" (Ref. 6). Hence, an I filter placed over the CCD array would serve to limit the wings of the CCD response and still provide adequate through-put for sensitivity.

(4) Information exists for converting V magnitudes to I magnitudes. The transformation requires only spectral type and luminosity class - both readily available from SKYMAP.

In the ideal case, the set of detectable stars exactly matches the catalog. Since this is not possible, it is desirable to maximize the completeness of the catalog to some rather faint magnitude to insure that most detectable stars are contained. It is important to note that stars which are faint in V may be relatively brighter at red wavelengths. As will be demonstrated in the next sections, a limit of magnitude 5 in I seems to be a reasonable limit for the CCD configuration assumed for the present study. The 8th magnitude limit of SKYMAP assures that the mission catalog listing will be sufficient.

2.2.2 The I Magnitude Conversion Method

Two external items of information are needed for the magnitude conversion. Values of $V_{abs} - I_{abs}$ were obtained from Johnson [7], whose table contains listings for three luminosity classes (I, III, & V - super giants, giants and main sequence) and extends over most spectral types.

The second value needed is a_I/a_V, the ratios of absorption in I to absorption in V, expressed in magnitude and as a function of spectral type by

$$\frac{a_I}{a_V} = \frac{\log_{10}[(\int_o^\infty I(\lambda)E(\lambda)(1 - \bar{I}(\lambda)d\lambda)/(\int_o^\infty I(\lambda)E(\lambda)d\lambda)]}{\log_{10}[(\int_o^\infty V(\lambda)E(\lambda)(1 - \bar{I}(\lambda)d\lambda)/(\int_o^\infty V(\lambda)E(\lambda)d\lambda)]} \qquad (2.1)$$

Where $I(\lambda)$ and $V(\lambda)$ are the filter responses, $E(\lambda)$ is the star energy function and $\bar{I}(\lambda)$ is the relative absorption function and λ is the wavelength. (see SKYMAP discription [5] for details). As pointed out in SKYMAP, this ratio is nearly constant over spectral type for narrow or intermediate band filters. To calculate this ratio the Planck energy function was used to model the stellar flux. Although this is not precisely valid, forming the ratio should lead to quite accurate results. The temperatures used were those given by Johnson [7] and no distinction was made by luminosity class. The values for absorption were taken from Figure 3.2 in the SKYMAP description by assuming absorption in magnitude is a linear function of wavelength over the range of interest (4800 Å - 10000 Å),

$$a(\lambda) = 1.77 \times 10^{-4} \times \lambda(\text{Å}) + 1.77, \qquad (2.4)$$

Where $a(\lambda)$ is absorption in magnitude at wavelength λ. The results of these calculations were that a_I/a_V varied from 0.25 to 0.32. The same value of a_I/a_V was used for I, III and V luminosity class stars at a given spectral type.

2.2.3 SKYMAP DATA

The data from SKYMAP needed for the magnitude conversion consists of apparant visual magnitude, spectral type, luminosity class and absorption in V. These data, with the exception of a_V, are given for

difficult in light of the complicated stellar spectral features in the blue wavelength region. A detailed description of the spectra would be requied. The I filter, on the other hand, is confined to the red wavelengths where the star spectra are relatively smooth.

(3) The I filter response peak is near that of typical CCD's. In addition, it overlaps the main peaks of the commonly accepted "typical CCD response" (Ref. 6). Hence, an I filter placed over the CCD array would serve to limit the wings of the CCD response and still provide adequate through-put for sensitivity.

(4) Information exists for converting V magnitudes to I magnitudes. The transformation requires only spectral type and luminosity class - both readily available from SKYMAP.

In the ideal case, the set of detectable stars exactly matches the catalog. Since this is not possible, it is desirable to maximize the completeness of the catalog to some rather faint magnitude to insure that most detectable stars are contained. It is important to note that stars which are faint in V may be relatively brighter at red wavelengths. As will be demonstrated in the next sections, a limit of magnitude 5 in I seems to be a reasonable limit for the CCD configuration assumed for the present study. The 8th magnitude limit of SKYMAP assures that the mission catalog listing will be sufficient.

2.2.2 The I Magnitude Conversion Method

Two external items of information are needed for the magnitude conversion. Values of $V_{abs} - I_{abs}$ were obtained from Johnson [7], whose table contains listings for three luminosity classes (I, III, & V - super giants, giants and main sequence) and extends over most spectral types.

most stars. It was necessary to collapse catagorses of luminosity class and some spectral types since the table from Johnson is limited. Collapsing is justified in most cases because either the catagory contains few stars and/or the properties are similar to those of listed star types. The following combinations were used:

R, N, C, S	Luminosity class III, spectral type M (all are variants of M III)
WR, WC, WN	Lum class III, spectral type 09 (all are hot giant stars similar to 09)
IV, III, II	III
V, VI	V
I, $I_{a'ab'b}$	I

No Luminosity class → V (most stars are V stars)

No subinterval in spectral type → 5 (i.e., A becomes A5)

No absorption given → set to 0

No spectral type → exclude

No m_V → exclude

Given the spectral type and luminosity class, the value of $V_{abs} - I_{abs}$ and a_I/a_V were found by interpolation in the table. Then:

$$m_I = m_V - (V_{abs} - I_{abs}) - a_V(1 - a_I/a_V), \qquad (2.5)$$

where m_V and a_V are from SKYMAP.

SKYMAP contains approximately 45,000 stars. Of these, 37 were not processed due to missing spectral type or visual magnitude.

2.2.4 Magnitude Limit of CCD Sensor

In order to establish a reasonable magnitude limit for a CCD sensor we 1) determine the flux in the filter bandpass for some standard star at the earth's atmosphere, and 2) multiply by appropriate factors dictated by the sensor.

The most direct way to obtain a flux estimate would be to observe known stars from space with the CCD sensor. Barring this, ground-based observations of stars with varying zenith angles could yield flux estimates outside the earth's atmosphere.

Our approximate method was to numerically integrate the surface flux distribution of a K7 V star model atmosphere over the I bandpass. The absolute I magnitude of such a star is approximately 6.2 (V = 8.1, V - I = 1.93). The radius is given by $\log R^*/R_{sun} = -0.11$ where $R_{sun} = 6.96 \times 10^{10}$cm. The surface flux is scaled by $(\frac{R^*}{R_{sun}} \times \frac{R_{sun}}{10_{pc}})^2 = 3.08 \times 10^{-18}$ where $1_{pc} = 3.08 \times 10^{17}$cm. The result of integrating and scaling is:

~1024 photons/cm^{2}sec.

Typical scale factors are:

-Lens area: 26.7 cm^2

-CCD response peak efficiency = .60

-I filter transmission peak efficiency = 0.85

-CCD effective area utilization = 0.46
(based on Fairchild 488 x 380 cell CCD)

-Integration time = 0.1 sec.

If we desire a minimum of 7500 photons/star for a sufficient signal-to-noise ratio, we compute the I magnitude limit of:

$$m_{limit} = 6.2 + 2.5 \log \frac{641}{7500}$$

$$= 3.5$$

Note that many factors are uncertain or could be altered. Integration time could be increased to 1 sec to give a limit of 6.0. We have chosen 5.0 to be the cutoff magnitude since this seems obtainable and gives approximately 5400 stars, a sufficient number for the pattern recognition process to work reliably.

We also note that model atmospheres for a variety of spectral types could be used to repeat the above calculation to yield a more precise magnitude limit.

The magnitude limit is flexible since the integration time for the star sensor is variable over a wide range. If the integration time is changed by a factor of 10 the magnitude limit is changed by 2.5 mag. In addition, the dynamic range of typical CCD arrays is 200 or about 6 magnitudes. The response is linear over the range to allow accurate magnitude calibration and detection.